



A versatile implicit computational framework for continuum-kinematics-inspired peridynamics

S. Firooz¹ · A. Javili² · P. Steinmann^{1,3}

Received: 31 July 2023 / Accepted: 18 October 2023
© The Author(s) 2023

Abstract

Continuum-kinematics-inspired peridynamics (CPD) has been recently proposed as a novel reformulation of peridynamics that is characterized by one-, two- and three-neighbor interactions. CPD is geometrically exact and thermodynamically consistent and does not suffer from zero-energy modes, displacement oscillations or material interpenetration. In this manuscript, for the first time, we develop a computational framework furnished with automatic differentiation for the implementation of CPD. Thereby, otherwise tedious analytical differentiation is automatized by employing hyper-dual numbers (HDN). This differentiation method does not suffer from round-off errors, subtractive cancellation errors or truncation errors and is thereby highly stable with superb accuracy being insensitive to perturbation values. The computational framework provided here is compact and model-independent, thus once the framework is implemented, any other material model can be incorporated via modifying the potential energy solely. Finally, to illustrate the versatility of our proposed framework, various potential energies are considered and the corresponding material response is examined for different scenarios.

Keywords Nonlocal elasticity · Peridynamics · Automatic differentiation · Hyper-dual numbers

1 Introduction

The main objective of this contribution is to establish a computational framework for CPD that is versatile and devoid of—often overly complex—analytical derivatives for residuals and tangents using HDN. A brief overview of CPD and HDN are given in Sects. 1.1 and 1.2, respectively. Section 1.3 elaborates on the key features of the manuscript. The notations and definitions that are employed throughout the manuscript are listed in Sect. 1.4, followed by Sect. 1.5 explaining the organization of the remainder of the manuscript.

1.1 Peridynamics

Peridynamics (PD) is a nonlocal framework to formulate continuum mechanics which assumes that physical points within a continuum body interact with each other across a finite distance called horizon [1]. In PD, the governing equations are formulated based on integral equations without spatial derivatives, which makes the framework suitable for the analysis of problems involving discontinuities and singularities such as fracture [2–9]. However, the spectrum of PD applications is considerably broad and not limited to fracture mechanics, see Javili et al. [10] for a comprehensive review. In bond-based PD, the interaction between two points within the continuum is only described by a two-point force density vector. Such simplified assumption for the interactions leads to failure in capturing the Poisson's effect. That is, the Poisson's ratio is restricted to 1/4 for isotropic materials. To overcome this limitation, state-based PD was developed [3] where the force density vector can be defined based on the stress tensors which allows the use of constitutive models in PD [11]. Recently, Javili et al. [12] established an alternative formulation for PD called “*continuum-kinematics-inspired peridynamics (CPD)*” wherein the underlying kinematics are reminiscent to classical continuum mechanics. The nonlocal

✉ S. Firooz
soheil.firooz@fau.de

¹ Institute of Applied Mechanics, Friedrich–Alexander Universität Erlangen–Nürnberg, Egerland Str. 5, 91058 Erlangen, Germany

² Department of Mechanical Engineering, Bilkent University, 06800 Ankara, Turkey

³ Glasgow Computational Engineering Centre, James Watt School of Engineering, University of Glasgow, Glasgow G12 8QQ, UK

material behavior in CPD is governed by three interactions types; one-neighbor interaction which occurs between a point and all of its neighbors; two-neighbor interaction which occurs between a point and all pairs of its neighbors; and three neighbor interaction which occurs between a point and all triplets of its neighbors. Since the interactions are defined by the change of pair-length, triplet-area and tetrad-volume, CPD build upon classical continuum mechanics kinematics. Additionally, constrained Poisson's ratio or zero-energy modes are absent in CPD. Owing to its great versatility and advantages, CPD has been growing rapidly. The computational framework for the implementation of CPD was developed in [13], see also [14]. Afterwards, Javili et al. [15] investigated the thermodynamic restrictions on the interaction energies in CPD and derived thermodynamically consistent constitutive laws through a Coleman–Noll-like procedure. Schaller et al. [16] reexamined the governing equations in CPD for open systems and demonstrated how the balances of momentum, energy and entropy are modified in the presence of an additional mass source. Zhou and Tian [17] investigated the concept of constitutive correspondence in CPD. Ekiz et al. [18, 19] established relationships between the material parameters of CPD and isotropic linear elasticity. For further studies on CPD, the reader is referred to the following references with applications to wrinkling and instabilities [20], bone remodeling [21], elasto-plasticity [22], damage and fracture [23, 24] and interfacial modeling in multi-phase materials [25, 26].

1.2 Hyper-dual numbers

In computational mechanics, modeling and simulation of the mechanical behavior of materials undergoing large deformations is a challenging task. Further complexities arise if accounting for inelasticity or anisotropy is required. The material behavior is commonly described by a potential energy function whose derivatives with respect to certain fields yields the stresses and tangent moduli. Accurate calculation of derivatives of the potential energy function is essential and considerably influences the simulation results. In particular, accurate calculation of the residual guarantees the precision in the physics of the problem and accurate calculation of the tangent influences the convergence of the Newton–Raphson scheme for solving the nonlinear system of equations [27, 28].

There exist various methods for the calculation of derivatives. At this stage of development on the subject, it seems virtually impossible to propose a classification that precisely addresses all aspects objectively. However, for the sake of representation and better conveying the ideas of the manuscript, we aim to propose a somewhat fair classification. Figure 1 shows a schematic classification of the

differentiation schemes.¹ The first differentiation scheme is approximate differentiation which is mainly numerical and is based on the Taylor series expansion [29]. A well-known example of approximate differentiation is the finite difference method which is usually classified, for example, into the backward, forward or central difference method. However, finite difference methods have two major drawbacks; first, they are approximations in essence and second, the derivative accuracy depends on the perturbation values. Small perturbations could yield instabilities due to machine precision and large perturbations yield inaccuracy especially for the second-order derivatives. Aside from the finite difference method, the complex-step derivative approximation method [30, 31], the double number method [32] have been proposed which do not suffer from the aforementioned disadvantages, see [33–39] for further studies on both methods. The second differentiation scheme is accurate differentiation which calculates the differentiation precisely. The first and most-well known accurate differentiation scheme is the analytical differentiation which is an ideal method due to its efficiency. However, for complex material models such as anisotropic materials, analytical calculation of derivatives can become excessively complicated and is an arduous task, if not impossible. In such cases, symbolic and automatic differentiations become handy since they are computer based [40]. Recently Fike and Alonso [41], based on the theory of quaternions developed by Clifford [42], developed an automatic differentiation tool employing “*hyper-dual numbers*” for the exact calculation of first and second derivatives, see also [43]. Hyper-dual numbers (HDN) are basically an extension of the dual numbers which are able to calculate the up to the second-derivatives precisely. Due to their promising accuracy and versatility, hyper-dual numbers (HDN) have been utilized in various research areas. Fundamentals of matrix representation of hyper-dual numbers were presented by Imot et al. [44] where higher-order derivatives could be calculated using hyper-dual numbers. Cohen and Shoham [45] introduced the algebra of hyper-dual numbers and hyper-dual vectors of higher orders. Endo et al. [46] developed a new variant of hyper-dual numbers called diagonal hyper-dual numbers which are computationally more efficient for the calculation of Hessian matrices. Kiran and Khandelwal [47] utilized hyper-dual numbers in finite strain anisotropic hyperelasticity in order to automatically calculate the Piola stress tensor and the corresponding tangent moduli from the potential energy function. A similar study was carried out by Tanaka et al. [48] for elasto-plasticity, who compared the performance of the incremental variational

¹ The term “accurate” in accurate differentiation in fact implies precise with no truncation or round-off errors. Finite difference methods can also have subsets based on their order of “accuracy” but it does not mean accurate in the sense of our accurate category.

formulation and hyper-dual numbers, see also [49]. Further studies with applications to hyper-dual numbers include rigid body kinematics [50–52], modelling equations of state [53], reduced order modeling [54], plate and shell buckling [55], gradient-enhanced elasto-plasticity [56] and topology optimization [57, 58].

1.3 Objectives and key features

CPD is a novel continuum formulation to explain the non-local behavior of materials. However, further exploration is required to fully grasp its potential. As any novel model, a crucial aspect to harness the capabilities of CPD lies in evaluating its utility to predict the material response for a wide range of energy densities and to identify their key properties. On the other hand - even for fairly simple energy densities - the derivations of the residuals and tangents in CPD become lengthy and intricate. This, in turn makes the computational implementation of CPD cumbersome and prone to errors. This manuscript aims to facilitate investigating arbitrary energies via a versatile framework that remains independent of the given energy model. To do so, we develop a computational framework furnished with automatic differentiation for a generic implementation of CPD via employing hyper-dual numbers (HDN). Although the governing equations of CPD are in integral form, calculation of derivatives are necessary to solve the system of non-linear equations in an implicit manner. In addition, the accuracy of the derivative calculation is important since it might influence the solution path in the case of non-convex potential energy functions [59] that can be encountered when modeling various physical phenomena such as in multi-scale modeling of carbon nano-tube foams [60], bi-stable elastic structures [61], mechanical transmission lines [62], narrow magnetic domain materials [63] and chemical surface adsorption [64]. Very few studies have been carried out on automatic differentiation methods in peridynamics [65–68]. However, to the best of the authors’ knowledge, there exist no contribution on implementation of hyper-dual numbers for CPD. Such computational framework paves the way for analysis of a wide range peridynamics material models which provides significant insights towards better understanding of complex material behaviors such as anisotropic materials or composites.

1.4 Notations and definitions

Throughout this manuscript, scalars are denoted by lower case Greek letters, first-order tensor quantities are denoted by lowercase bold letters and second-order tensor quantities are denoted by uppercase bold letters. For instance α is a scalar, \mathbf{a} is a first-order tensor, \mathbf{A} is a second-order tensor. The cross product of two vectors \mathbf{a} and \mathbf{b} is a vector $\mathbf{c} = \mathbf{a} \times \mathbf{b}$

with $[\mathbf{c}]_k = [\mathbf{a}]_i [\mathbf{b}]_j [\epsilon]_{ijk}$ where $[\epsilon]_{ijk}$ is the third-order Levi-Civita permutation tensor. The action of a second-order tensor \mathbf{A} on a vector \mathbf{b} results in a vector $\mathbf{c} = \mathbf{A} \cdot \mathbf{b}$ with $[\mathbf{c}]_i = [\mathbf{A}]_{ij} [\mathbf{b}]_j$. The standard dot product of a vector \mathbf{a} to a third-order tensor \mathfrak{a} results in a second-order tensor $\mathbf{A} = \mathbf{a} \cdot \mathfrak{a}$ with $[\mathbf{A}]_{ij} = [\mathbf{a}]_k [\mathfrak{a}]_{kij}$. The non-standard dot product of a vector \mathbf{a} to a third-order tensor \mathfrak{a} results in a second-order tensor $\mathbf{A} = \mathbf{a} \cdot \mathfrak{a}$ with $[\mathbf{A}]_{ij} = [\mathbf{a}]_k [\mathfrak{a}]_{ikj}$. The imaginary (non-real) and the real operators are denoted as \Im and \Re . For instance, for an arbitrary complex number $\alpha + \beta i$, the imaginary (non-real) operator \Im extracts the imaginary part as $\Im(\alpha + \beta i) = \beta$ and the real operator extracts the real part as $\Re(\alpha + \beta i) = \alpha$. As will be discussed later, for double numbers, dual numbers and hyper-dual numbers, the non-real unit has different properties than the well-known imaginary unit i and shall generally be addressed as a non-real unit. To avoid confusing terminologies, we also refer to the imaginary unit i as non-real.

1.5 Organization of the manuscript

The remainder of the manuscript is organized as follows. In Sect. 2, the fundamentals of CPD and its computational implementation are briefly reviewed. Hyper-dual numbers and their algebra are introduced in Sect. 3 where numerical differentiation using hyper-dual numbers with respect to scalar, vector and tensor arguments is elaborated. In Sect. 4, CPD is furnished with hyper-dual numbers and a general framework for calculation of the residual and tangents in CPD is developed. Section 5 details on a family of potential energy functions employed in this manuscript. The proposed framework is evaluated through a set of numerical examples in Sect. 6. Finally, Sect. 7 concludes the work and provides further outlooks. Table 1 summarizes the notation and terminology adopted in this manuscript.

2 Continuum-kinematics-inspired peridynamics

2.1 Kinematics

Let \mathcal{B}_0 be a continuum body with material configuration at time $t = 0$ which is mapped to its spatial counterpart \mathcal{B}_t via the nonlinear deformation map as $\mathbf{x} = \mathbf{y}(\mathbf{X}, t)$, as shown in Fig. 2. In the material configuration, the point \mathbf{X}^a interacts with its neighbors $\mathbf{X}^i, \mathbf{X}^j, \mathbf{X}^k$, etc within the Horizon \mathcal{H}_0 . Similarly, the point \mathbf{x}^a interacts with its mapped neighbors $\mathbf{x}^i, \mathbf{x}^j, \mathbf{x}^k$, etc within the Horizon \mathcal{H}_t . The relative positions between the points and their neighbors in the material and spatial configurations are defined as

$$\mathfrak{E}^{ai} := \mathbf{X}^i - \mathbf{X}^a \quad \text{and} \quad \mathfrak{e}^{ai} := \mathbf{x}^i - \mathbf{x}^a = \mathbf{y}(\mathbf{X}^i) - \mathbf{y}(\mathbf{X}^a). \tag{1}$$

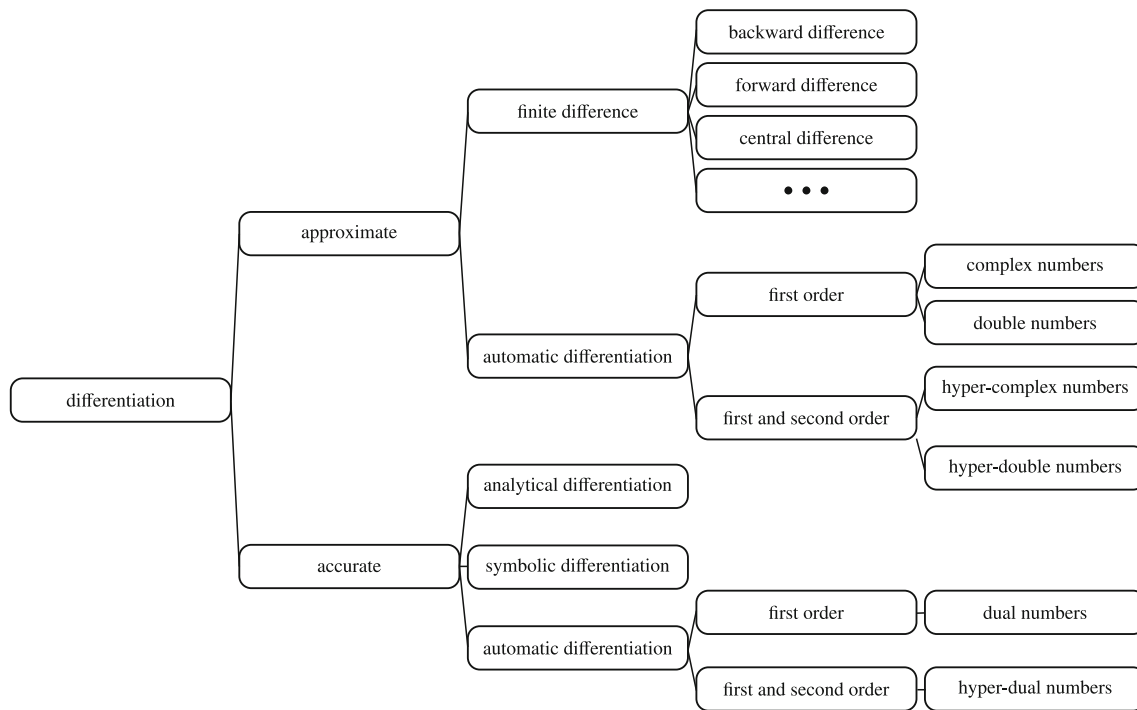


Fig. 1 A classification of the differentiation schemes. Note that such a classification is introduced for the sake of representation and better conveying the ideas of the manuscript

Similar to classical continuum mechanics, there exist three relative deformation measures in CPD. The first relative deformation measure is the relative position vector ξ^{ai} which describes one-neighbor interactions and is defined as

$$\xi^{ai} := \mathbf{x}^i - \mathbf{x}^a. \quad (2)$$

This relative deformation measure mimics the deformation gradient \mathbf{F} which maps infinitesimal material line elements $d\mathbf{X}$ to their spatial counterparts $d\mathbf{x}$. Note, the superscript “ ai ” implies that the relative position vector corresponds to points $\{a, i\}$ and shall not be confused with tensor indices. The second relative deformation measure is the relative area vector \mathbf{a}^{aij} which describes two-neighbor interactions and is defined as

$$\mathbf{a}^{aij} := [\mathbf{x}^i - \mathbf{x}^a] \times [\mathbf{x}^j - \mathbf{x}^a] = \xi^{ai} \times \xi^{aj}. \quad (3)$$

This relative deformation measure mimics the cofactor of the deformation gradient $\text{Cof} \mathbf{F} = \mathbf{J} \mathbf{F}^{-T}$ which maps infinitesimal material area elements $d\mathbf{A}$ to their spatial counterparts $d\mathbf{a}$. Similarly, the superscript “ aij ” implies that the area is spanned between points $\{a, i, j\}$ and shall not be confused with tensor indices. The third relative deformation measure is the relative volume v^{aijk} which describes three-neighbor interactions and is defined as

$$v^{aijk} := \left[\left[\mathbf{x}^i - \mathbf{x}^a \right] \times \left[\mathbf{x}^j - \mathbf{x}^a \right] \right] \cdot \left[\mathbf{x}^k - \mathbf{x}^a \right]$$

$$\cdot \left[\mathbf{x}^k - \mathbf{x}^a \right] = \left[\xi^{ai} \times \xi^{aj} \right] \cdot \xi^{ak}. \quad (4)$$

This relative deformation measure mimics the determinant of the deformation gradient $\mathbf{J} = \text{Det}(\mathbf{F})$ which maps infinitesimal material volume elements dV to their spatial counterparts dv . The superscript “ $aijk$ ” implies that the volume is spanned between points $\{a, i, j, k\}$ and shall not be confused with tensor indices. In the limit of vanishing horizon the following relations hold between the relative deformation measures

$$\left. \begin{aligned} \xi^{ai} &:= \mathbf{x}^i - \mathbf{x}^a \\ \mathbf{a}^{aij} &:= \xi^{ai} \times \xi^{aj} \\ v^{aijk} &:= \left[\xi^{ai} \times \xi^{aj} \right] \cdot \xi^{ak} \end{aligned} \right\} \xrightarrow{\delta_0 \rightarrow 0} \begin{cases} \xi^{ai} := \mathbf{F} \cdot \Xi^{ai} \\ \mathbf{a}^{aij} := \text{Cof} \mathbf{F} \cdot \mathbf{A}^{aij} \\ v^{aijk} := \text{Det} \mathbf{F} V^{aijk} \end{cases}. \quad (5)$$

2.2 Governing equations

The next step is to elaborate the governing equations. In order to obtain the governing equations, the total potential energy functional is minimized via setting its variation to zero. The total potential energy Π is composed of the internal potential energy Ψ and the external potential energy Υ as

$$\Pi = \Psi + \Upsilon \quad \implies \quad \delta \Pi = \delta \Psi + \delta \Upsilon \quad \forall \delta \mathbf{y}. \quad (6)$$

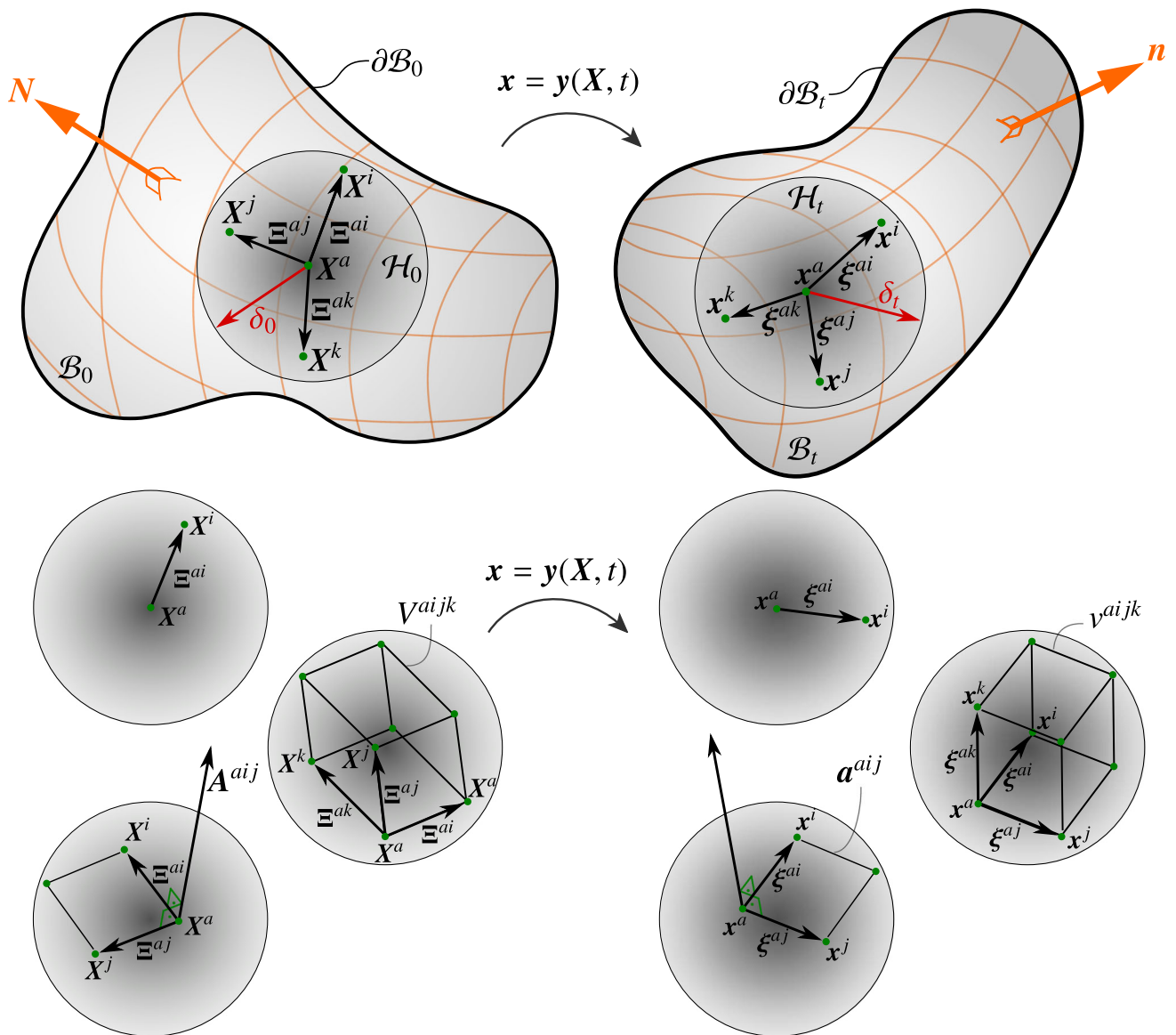


Fig. 2 Problem definition in CPD. A continuum body B_0 in the material configuration is mapped to its spatial counterpart B_t via the nonlinear deformation map y . The point a interacts with its neighbors within a horizon \mathcal{H}_0 and \mathcal{H}_t in both material and spatial configurations, respectively. There exist three interaction types in CPD. One-, two-

and three-neighbor interactions which correspond to the relative position vector, area and volume, respectively. ξ^{ai} is the relative position between the points a, i . A^{aij} is the area formed between the points a, i, j . V^{aijk} is the volume formed between the points a, i, j, k

It shall be noted that our analysis will be carried out for non-dissipative processes in a variational setting. The variation of the external potential energy reads

$$\delta\Upsilon = - \int_{B_0} \mathbf{b}_{\text{ext}}^a \cdot \delta \mathbf{y}^a \, dV - \int_{\partial B_0} \mathbf{t}_{\text{ext}}^b \cdot \delta \mathbf{y}^b \, dA, \quad (7)$$

with $\mathbf{b}_{\text{ext}}^a$ being the external force density and $\mathbf{t}_{\text{ext}}^a$ being the external traction on the boundary.

2.2.1 Internal potential energy

The internal potential energy consists of the contribution of one-, two- and three-neighbor interactions as

$$\begin{aligned} \Psi = \Psi_1 + \Psi_2 + \Psi_3 = & \int_{B_0} \left[\frac{1}{2} \int_{\mathcal{H}_0} \psi_1^{ai} \, dV_1 \right. \\ & \left. + \frac{1}{3} \iint_{\mathcal{H}_0} \psi_2^{aij} \, dV_2 \, dV_1 \frac{1}{4} \iiint_{\mathcal{H}_0} \psi_3^{aijk} \, dV_3 \, dV_2 \, dV_1 \right] dV. \end{aligned} \quad (8)$$

The factors 1/2, 1/3 and 1/4 are associated with equivalent energies encountered for the same pairs, triplets and quadruples, respectively. The variation of the internal potential energy reads

$$\begin{aligned} \delta\Psi_1 &= \int_{\mathcal{B}_0} \int_{\mathcal{H}_0} \delta\psi_1^{ai} dV_1 dV, \\ \delta\Psi_2 &= \int_{\mathcal{B}_0} \iint_{\mathcal{H}_0} \delta\psi_2^{aij} dV_2 dV_1 dV, \\ \delta\Psi_3 &= \int_{\mathcal{B}_0} \iiint_{\mathcal{H}_0} \delta\psi_3^{aijk} dV_3 dV_2 dV_1 dV, \end{aligned} \tag{9}$$

where the pre-factors disappear. The one-, two- and three-neighbor interactions potential energy densities are a function of the relative position vector between point a and its neighbor i , the area vector formed by point a and its neighbor pairs $\{i, j\}$ and the volume formed by point a and its

neighbor triplets $\{i, j, k\}$, respectively, as

$$\begin{aligned} \psi_1^{ai} &= \psi_1^{ai}(\xi^{ai}), \\ \psi_2^{aij} &= \psi_2^{aij}(\mathbf{a}^{aij}), \\ \psi_3^{aijk} &= \psi_3^{aijk}(v^{aijk}). \end{aligned} \tag{10}$$

Using the relation $\delta\xi^{ai} = \delta y^i - \delta y^a$ and the following identities

$$\begin{aligned} \delta\xi^{ai} &= \delta y^i - \delta y^a, \\ \delta\mathbf{a}^{aij} &= [\delta\xi^{ai} \times \xi^{aj}] + [\xi^{ai} \times \delta\xi^{aj}], \\ \delta v^{aijk} &= [\delta\xi^{ai} \times \xi^{aj}] \cdot \xi^{ak} + [\xi^{ai} \times \delta\xi^{aj}] \cdot \xi^{ak} \\ &\quad + [\xi^{ai} \times \xi^{aj}] \cdot \delta\xi^{ak}, \end{aligned} \tag{11}$$

Table 1 Summary of notation and terminology

Nomenclature			
δ	Kronecker delta	ϵ	Third-order Levi-Civita permutation tensor
\mathbf{X}^i	Material position vector of point i	\mathbf{x}^i	Spatial position vector of point i
Π	Total potential energy	ξ^{ai}	Spatial relative position vector between points $\{a, i\}$
Ψ	Total internal potential energy	\mathbf{a}^{aij}	Spatial area vector spanned between points $\{a, i, j\}$
Υ	Total external potential energy	v^{aijk}	Spatial volume formed by points $\{a, i, j, k\}$
δ_0	Material horizon size	Ξ^{ai}	Material relative position vector between points $\{a, i\}$
δ_r	Spatial horizon size	\mathbf{A}^{aij}	Material area vector spanned between points $\{a, i, j\}$
\mathbf{y}	Non-linear deformation map	V^{aijk}	Material volume formed by points $\{a, i, j, k\}$
$\nu^{\mathcal{H}}$	volume of the horizon	\mathbf{p}^{ai}	Internal force density per volume squared between points $\{a, i\}$
ν^i	Volume assigned to each neighbor	$\mathbf{b}_{\text{int}}^a$	point-wise internal force density per volume for point a
$\#\mathcal{P}$	Number of collocation points	$\mathbf{b}_{\text{ext}}^a$	Point-wise external force density per volume for point a
$\#\mathcal{N}$	Number of neighbors	$\mathbf{t}_{\text{ext}}^a$	Point-wise external traction on the boundary for point a
\mathbf{x}	Global position vector	\mathbf{x}^a	Point-wise position vector for point a
\mathbb{R}	Global residual vector	\mathbf{R}^a	Point-wise residual vector for point a
\mathbb{K}	Global tangent matrix	\mathbf{K}^{ab}	Point-wise stiffness matrix for points a and b
C_1	One-neighbor elastic coefficient	ψ_1^{ai}	One-neighbor interaction energy density
C_2	Two-neighbor elastic coefficient	ψ_2^{aik}	Two-neighbor interaction energy density
C_3	Three-neighbor elastic coefficient	ψ_3^{aijk}	Three-neighbor interaction energy density
\Re	Real operator	\Im	Imaginary or non-real operator
\hat{a}	Hyper-complex number	i_1	First non-real part of hyper-complex numbers
$\hat{\mathbf{a}}$	Hyper-complex vector	i_2	Second non-real part of hyper-complex numbers
$\hat{\mathbf{A}}$	Hyper-complex second-order tensor	i_{12}	Third (mixed) non-real part of hyper-complex numbers
\tilde{a}	Hyper-double number	e_1	First non-real part of hyper-double numbers
$\tilde{\mathbf{a}}$	Hyper-double vector	e_2	Second non-real part of hyper-double numbers
$\tilde{\mathbf{A}}$	Hyper-double second-order tensor	e_{12}	Third (mixed) non-real part of hyper-double numbers
\bar{a}	Hyper-dual number	ϵ_1	First non-real part of hyper-dual numbers
$\bar{\mathbf{a}}$	Hyper-dual vector	ϵ_2	Second non-real part of hyper-dual numbers
$\bar{\mathbf{A}}$	Hyper-dual second-order tensor	ϵ_{12}	Third (mixed) non-real part of hyper-dual numbers

the final form of the variation of the internal potential energy variation reads

$$\delta\Psi = \underbrace{\int_{\mathcal{B}_0} \int_{\mathcal{H}_0} \left[\frac{\partial\psi_1^{ai}}{\partial\xi^{ai}} + \int_{\mathcal{H}_0} \left[2\xi^{aj} \times \frac{\partial\psi_2^{aij}}{\partial\mathbf{a}^{aij}} \right] dV_2 + \iint_{\mathcal{H}_0} \left[3 \frac{\partial\psi_3^{aijk}}{\partial v^{aijk}} \left[\xi^{aj} \times \xi^{ak} \right] \right] dV_3 dV_2 \right]}_{\mathbf{p}^{ai}} \cdot \delta\mathbf{y}^i dV_1 dV + \underbrace{- \int_{\mathcal{B}_0} \left[\int_{\mathcal{H}_0} \frac{\partial\psi_1^{ai}}{\partial\xi^{ai}} dV_1 + \iint_{\mathcal{H}_0} \left[2\xi^{aj} \times \frac{\partial\psi_2^{aij}}{\partial\mathbf{a}^{aij}} \right] dV_2 dV_1 + \iiint_{\mathcal{H}_0} \left[3 \frac{\partial\psi_3^{aijk}}{\partial v^{aijk}} \left[\xi^{aj} \times \xi^{ak} \right] \right] dV_3 dV_2 dV_1 \right]}_{\mathbf{b}_{\text{int}}^a} \cdot \delta\mathbf{y}^a dV, \tag{12}$$

with \mathbf{p}^{ai} being the force density per volume squared and $\mathbf{b}_{\text{int}}^a$ being the internal force density per volume. Thus, the compact form of the internal potential energy potential variation boils down to

$$\delta\Psi = \int_{\mathcal{B}_0} \int_{\mathcal{H}_0} \mathbf{p}^{ai} \cdot \delta\mathbf{y}^i dV_1 dV - \int_{\mathcal{B}_0} \mathbf{b}_{\text{int}}^a \cdot \delta\mathbf{y}^a dV. \tag{13}$$

2.2.2 Equilibrium and balance equations

Via setting the variation of the total potential energy with respect to admissible variations $\delta\mathbf{y}$ at a fixed material point to zero, the governing equations for equilibrium are obtained. Inserting Eqs. (13) and (7) into Eq. (6) yields

$$\int_{\mathcal{B}_0} \int_{\mathcal{H}_0} \mathbf{p}^{ai} \cdot \delta\mathbf{y}^i dV_1 dV - \int_{\mathcal{B}_0} \mathbf{b}_{\text{int}}^a \cdot \delta\mathbf{y}^a dV - \int_{\mathcal{B}_0} \mathbf{b}_{\text{ext}}^a \cdot \delta\mathbf{y}^a dV - \int_{\partial\mathcal{B}_0} \mathbf{t}_{\text{ext}}^b \cdot \delta\mathbf{y}^b dA = 0. \tag{14}$$

Due to arbitrariness of $\delta\mathbf{y}$, we can readily extract the governing equations as

$$\int_{\mathcal{B}_0} \mathbf{b}_{\text{int}}^a dV + \int_{\mathcal{B}_0} \mathbf{b}_{\text{ext}}^a dV = \mathbf{0}, \quad \text{subject to} \\ \int_{\mathcal{B}_0} \int_{\mathcal{H}_0} \mathbf{p}^{ai} \cdot \delta\mathbf{y}^i dV_1 dV - \int_{\partial\mathcal{B}_0} \mathbf{t}_{\text{ext}}^b \cdot \delta\mathbf{y}^b dA = 0, \tag{15}$$

in global form and as

$$\mathbf{b}_{\text{int}}^a + \mathbf{b}_{\text{ext}}^a = \mathbf{0}, \tag{16}$$

in point-wise local form. The obtained relations formulate the linear momentum balance which is the underlying governing equation in CPD. The angular momentum balance is a priori satisfied if the internal potential energy densities sat-

isfy material frame indifference or more precisely, if they are defined as functions of $|\xi^{ai}|$, $|\mathbf{a}^{aij}|$ and, $|v^{aijk}|$.

2.3 Computational implementation of CPD

The first step towards computational implementation of CPD is to transform the equations from their continuous form to a discrete form. In doing so, the integrals over the horizon are transformed to summation over neighbors and using quadrature rule, integrals over the body are transformed to summation over collocation points. In our case, the collocation points and the quadrature points coincide, thus, we refer to them collectively as grid points henceforth, see [13].

For the linear momentum balance equation, we here assume that external body forces are zero for the sake of presentation. Accordingly the local form of the linear momentum balance can be expressed in discretized form as

$$\mathbf{b}_{\text{int}}^a = \sum_{i=1}^{\#\mathcal{N}} \frac{\partial\psi_1^{ai}}{\partial\xi^{ai}} \mathcal{V}^i + \sum_{i=1}^{\#\mathcal{N}} \sum_{\substack{j=1 \\ j \neq i}}^{\#\mathcal{N}} \left[2\xi^{aj} \times \frac{\partial\psi_2^{aij}}{\partial\mathbf{a}^{aij}} \right] \mathcal{V}^{ij} \\ + \sum_{i=1}^{\#\mathcal{N}} \sum_{\substack{j=1 \\ j \neq i}}^{\#\mathcal{N}} \sum_{\substack{k=1 \\ k \neq i \\ k \neq j}}^{\#\mathcal{N}} \left[3 \frac{\partial\psi_3^{aijk}}{\partial v^{aijk}} \left[\xi^{aj} \times \xi^{ak} \right] \right] \mathcal{V}^{ijk} = \mathbf{0}, \tag{17}$$

with $\mathcal{V}^i, \mathcal{V}^{ij}, \mathcal{V}^{ijk}$ accounting for volume integrals. We define the point-wise residual vector for collocation point \mathcal{P}^a as \mathbf{R}^a , which is composed of three parts; one-neighbor interactions contributions, two-neighbor interactions contributions and three-neighbor interactions contributions. That is

$$\mathbf{R}^a = \mathbf{R}_1^a + \mathbf{R}_2^a + \mathbf{R}_3^a = \mathbf{0}, \tag{18}$$

with

$$\mathbf{R}_1^a = \sum_{i=1}^{\#\mathcal{N}} \frac{\partial\psi_1^{ai}}{\partial\xi^{ai}} \mathcal{V}^i,$$

$$\begin{aligned}
 \mathbf{R}_2^a &= \sum_{i=1}^{\#\mathcal{N}} \sum_{\substack{j=1 \\ j \neq i}}^{\#\mathcal{N}} \left[2\xi^{aj} \times \frac{\partial \psi_2^{aj}}{\partial \mathbf{a}^{aj}} \right] \psi^{ij}, \\
 \mathbf{R}_3^a &= \sum_{i=1}^{\#\mathcal{N}} \sum_{\substack{j=1 \\ j \neq i}}^{\#\mathcal{N}} \sum_{\substack{k=1 \\ k \neq i \\ k \neq j}}^{\#\mathcal{N}} \left[3 \frac{\partial \psi_3^{ajk}}{\partial v^{ajk}} \left[\xi^{aj} \times \xi^{ak} \right] \right] \psi^{ijk}. \quad (19)
 \end{aligned}$$

The global discretized residual vector \mathbb{R} is composed of point-wise discretized residual vectors \mathbf{R}^a assembled into a global vector formally represented as $\mathbb{R} = [\mathbf{R}^1 \ \mathbf{R}^2 \ \dots \ \mathbf{R}^a \ \dots \ \mathbf{R}^{\#\mathcal{P}}]^T$. Similar to the point-wise residual, the point-wise tangent can be decomposed into three parts associated with one-, two- and three-neighbor interactions as $\mathbf{K}^{ab} = \partial \mathbf{R}^a / \partial \mathbf{x}^b = \mathbf{K}_1^{ab} + \mathbf{K}_2^{ab} + \mathbf{K}_3^{ab}$ with

$$\begin{aligned}
 \mathbf{K}_1^{ab} &= \frac{\partial \mathbf{R}_1^a}{\partial \mathbf{x}^b} = \frac{\partial}{\partial \mathbf{x}^b} \left(\sum_{i=1}^{\#\mathcal{N}} \frac{\partial \psi_1^{ai}}{\partial \xi^{ai}} \psi^i \right), \\
 \mathbf{K}_2^{ab} &= \frac{\partial \mathbf{R}_2^a}{\partial \mathbf{x}^b} = \frac{\partial}{\partial \mathbf{x}^b} \left(\sum_{i=1}^{\#\mathcal{N}} \sum_{\substack{j=1 \\ j \neq i}}^{\#\mathcal{N}} \left[2\xi^{aj} \times \frac{\partial \psi_2^{aj}}{\partial \mathbf{a}^{aj}} \right] \psi^{ij} \right), \\
 \mathbf{K}_3^{ab} &= \frac{\partial \mathbf{R}_3^a}{\partial \mathbf{x}^b} = \frac{\partial}{\partial \mathbf{x}^b} \left(\sum_{i=1}^{\#\mathcal{N}} \sum_{\substack{j=1 \\ j \neq i}}^{\#\mathcal{N}} \sum_{\substack{k=1 \\ k \neq i \\ k \neq j}}^{\#\mathcal{N}} \left[3 \left[\xi^{aj} \times \xi^{ak} \right] \frac{\partial \psi_3^{ajk}}{\partial v^{ajk}} \right] \psi^{ijk} \right). \quad (20)
 \end{aligned}$$

The fully discrete nonlinear system of governing equations can be stated as $\mathbb{R} \doteq \mathbf{0}$ which could be solved using an iterative Newton–Raphson scheme. The consistent linearization of the resulting system at iteration n reads

$$\begin{aligned}
 \mathbb{R}_{n+1} &= \mathbb{R}_n + \mathbb{K}_n \cdot \Delta \mathbf{x}_n \doteq \mathbf{0} \quad \text{thus} \\
 \Delta \mathbf{x}_n &= -\mathbb{K}_n^{-1} \cdot \mathbb{R}_n \quad \text{with} \quad \mathbb{K}_n := \left. \frac{\partial \mathbb{R}}{\partial \mathbf{x}} \right|_n, \quad (21)
 \end{aligned}$$

where $\Delta \mathbf{x}$ is the incremental global deformation vector. After each iteration, the global deformation vector \mathbf{x} is updated by $\Delta \mathbf{x}$ according to $\mathbf{x}_{n+1} = \mathbf{x}_n + \Delta \mathbf{x}_n$. Obviously, equations (19) and (20) require calculations of the first and second derivatives of the potential energy function, respectively, which is gathered in Table 2. Such calculations are carried out in a generic form using the hyper-dual numbers in the next Section.

Table 2 Derivatives required for calculation of the residual and tangents in CPD

$\frac{\partial \psi_1^{ai}}{\partial \xi^{ai}}$	$\frac{\partial}{\partial \mathbf{x}^b} \left(\frac{\partial \psi_1^{ai}}{\partial \xi^{ai}} \right) = \left[\frac{\partial^2 \psi_1^{ai}}{\partial \xi^{ai^2}} \right] \left[\frac{\partial \xi^{ai}}{\partial \mathbf{x}^b} \right]$
$\frac{\partial \psi_2^{aj}}{\partial \mathbf{a}^{aj}}$	$\frac{\partial}{\partial \mathbf{x}^b} \left(\frac{\partial \psi_2^{aj}}{\partial \mathbf{a}^{aj}} \right) = \left[\frac{\partial^2 \psi_2^{aj}}{\partial \mathbf{a}^{aj^2}} \right] \left[\frac{\partial \mathbf{a}^{aj}}{\partial \mathbf{x}^b} \right]$
$\frac{\partial \psi_3^{ajk}}{\partial v^{ajk}}$	$\frac{\partial}{\partial \mathbf{x}^b} \left(\frac{\partial \psi_3^{ajk}}{\partial v^{ajk}} \right) = \left[\frac{\partial^2 \psi_3^{ajk}}{\partial v^{ajk^2}} \right] \left[\frac{\partial v^{ajk}}{\partial \mathbf{x}^b} \right]$

3 Hyper-dual numbers

In computational mechanics, it is crucial to calculate the derivatives of the potential energy function accurately since it has a significant impact on simulation outcomes. Precise computation of the residual is particularly essential to ensure the accuracy of the physics involved in the problem, while calculating the tangent with precision affects the ability of the Newton–Raphson method to converge in solving the nonlinear system of equations. Numerical differentiation is a common technique to approximate the derivative of a function using various methods. One of the disadvantages of numerical differentiation methods compared to analytical differentiation is that they suffer from numerical errors. There exist two main sources of error in numerical differentiation. The first error type is the truncation error which arises when higher-order terms in approximations or derivative calculations are neglected. The truncation error can be minimized by making the perturbation value h very small. The second error type is the subtractive cancellation error which occurs because in computers the numbers are only stored up to a certain precision. For example, in double precision arithmetic, the numbers are stored up to 15 decimal digits. If the numbers that are being subtracted from each other are too close, the computer fails to distinguish them hence the zero difference. This leads to an incorrect approximation of the derivatives. The subtractive cancellation error increases by making the perturbation value h very small. Therefore, both errors cannot be minimized simultaneously via decreasing the perturbation value h . Various numerical differentiation techniques have been developed to minimize these errors, among which, hyper-dual numbers have proven to be one of the most accurate methods. Appendix A provides a unifying study on various numerical differentiation techniques and highlights the advantages and disadvantages of each method.

Hyper-dual numbers are a number system developed based on the theory of quaternions to calculate exact first and second derivatives. The derivation calculation involves converting a real-valued function evaluation to operate on hyper-dual numbers. The hyper-dual numbers are character-

ized by one real part and three non-real parts. A hyper-dual number \bar{a} is defined as

$$\begin{aligned} \bar{a} &= a_0 + a_1\epsilon_1 + a_2\epsilon_2 + a_{12}\epsilon_{12} \quad \text{with} \\ \epsilon_{12} &= \epsilon_{21} = \epsilon_1\epsilon_2 = \epsilon_2\epsilon_1 \neq 0 \quad \text{and} \quad \epsilon_1^2 = \epsilon_2^2 = 0. \end{aligned} \tag{22}$$

Accordingly, the real and non-real operators are defined as

$$\begin{aligned} \Re(\bar{a}) &= \Re(a_0 + a_1\epsilon_1 + a_2\epsilon_2 + a_{12}\epsilon_{12}) = a_0, \\ \Im_{\epsilon_1}(\bar{a}) &= \Im_{\epsilon_1}(a_0 + a_1\epsilon_1 + a_2\epsilon_2 + a_{12}\epsilon_{12}) = a_1, \\ \Im_{\epsilon_2}(\bar{a}) &= \Im_{\epsilon_2}(a_0 + a_1\epsilon_1 + a_2\epsilon_2 + a_{12}\epsilon_{12}) = a_2, \\ \Im_{\epsilon_{12}}(\bar{a}) &= \Im_{\epsilon_{12}}(a_0 + a_1\epsilon_1 + a_2\epsilon_2 + a_{12}\epsilon_{12}) = a_{12}. \end{aligned} \tag{23}$$

When operations are performed on the real component of a hyper-dual number, the derivative information for those operations is created and stored in the non-real parts of the number. The non-real elements of the number contain derivative information with regard to the input at every stage of the function evaluation. Cohen and Shoham [45] demonstrated that hyper-dual numbers are indeed an extended version of dual numbers of order two. For the sake of simplicity, it is usually assumed that $a_1 = a_2 = h$ and $a_{12} = 0$ hence $\bar{a} = a_0 + h\epsilon_1 + h\epsilon_2$. Therefore, the Taylor series expansion of the smooth function $f(x + h\epsilon_1 + h\epsilon_2)$ reads

$$\begin{aligned} f(x + h\epsilon_1 + h\epsilon_2) &= f(x) + h\epsilon_1 \frac{\partial f(x)}{\partial x} + h\epsilon_2 \frac{\partial f(x)}{\partial x} \\ &\quad + h^2\epsilon_{12} \frac{\partial^2 f(x)}{\partial x^2}, \end{aligned} \tag{24}$$

that could be rewritten as

$$\begin{aligned} f(x + h\epsilon_1 + h\epsilon_2) &= f(x) + \left[h \frac{\partial f(x)}{\partial x} \right] \epsilon_1 \\ &\quad + \left[h \frac{\partial f(x)}{\partial x} \right] \epsilon_2 + \left[h^2 \frac{\partial^2 f(x)}{\partial x^2} \right] \epsilon_{12}, \end{aligned} \tag{25}$$

The first and second derivatives of $f(x)$ can be calculated as

$$\begin{aligned} \frac{\partial f(x)}{\partial x} &= \frac{\Im_{\epsilon_1}(f(x + h\epsilon_1 + h\epsilon_2))}{h} \\ &= \frac{\Im_{\epsilon_2}(f(x + h\epsilon_1 + h\epsilon_2))}{h} \quad \text{and} \\ \frac{\partial^2 f(x)}{\partial x^2} &= \frac{\Im_{\epsilon_{12}}(f(x + h\epsilon_1 + h\epsilon_2))}{h^2}. \end{aligned} \tag{26}$$

Note that the operators \Im_{ϵ_1} , \Im_{ϵ_2} and $\Im_{\epsilon_{12}}$ extract the multiples to the non-real parts ϵ_1 , ϵ_2 and ϵ_{12} , respectively. It is observed that the first and the second derivatives neither suffer from

truncation errors nor from subtractive cancellation errors. As a result, both derivatives are calculated in an exact manner.

3.1 Algebra and tensor analysis with hyper-dual numbers

This section briefly elaborates the algebra of hyper-dual numbers. Table 3 summaries the definitions for basic algebraic operations for hyper-dual numbers. As mentioned in the previous section, it is usually assumed that for a typical hyper-dual number $a_1 = a_2 = h$ and $a_{12} = 0$. Therefore, a hyper-dual number can be represented as $\bar{a} = a_0 + h\epsilon_1 + h\epsilon_2$. Another equally important feature of differentiation with hyper-dual numbers is that the derivatives do not depend on the perturbation magnitude h , thus one could assume $h = 1$. Accordingly, we henceforth continue our analysis with hyper-dual numbers defined as $\bar{a} = a_0 + \epsilon_1 + \epsilon_2$. Assume that $f(x)$ is a scalar valued function of a scalar variable x . The first and second derivatives of $f(x)$ with respect to x can be obtained as

$$\begin{aligned} \frac{\partial f(x)}{\partial x} &= \Im_{\epsilon_1}(f(x + \epsilon_1 + \epsilon_2)) = \Im_{\epsilon_2}(f(x + \epsilon_1 + \epsilon_2)), \\ \frac{\partial^2 f(x)}{\partial x^2} &= \Im_{\epsilon_{12}}(f(x + \epsilon_1 + \epsilon_2)). \end{aligned} \tag{27}$$

Similarly, for a two variable scalar function $f(x, y)$, the derivatives with respect to scalar independent variables are obtained as

$$\begin{aligned} \frac{\partial f(x, y)}{\partial x} &= \Im_{\epsilon_1}(f(x + \epsilon_1, y + \epsilon_2)), \\ \frac{\partial f(x, y)}{\partial y} &= \Im_{\epsilon_2}(f(x + \epsilon_1, y + \epsilon_2)), \\ \frac{\partial^2 f(x, y)}{\partial x \partial y} &= \Im_{\epsilon_{12}}(f(x + \epsilon_1, y + \epsilon_2)), \\ \frac{\partial^2 f(x, y)}{\partial x^2} &= \Im_{\epsilon_{12}}(f(x + \epsilon_1 + \epsilon_2, y)), \\ \frac{\partial^2 f(x, y)}{\partial y^2} &= \Im_{\epsilon_{12}}(f(x, y + \epsilon_1 + \epsilon_2)). \end{aligned} \tag{28}$$

As shown in Eq. (28), in order to find the whole set of first and second derivatives, three different combinations of the hyper-dual forms for the independent variables need to be used. Thus, the function $f(x, y)$ needs to be evaluated three times.

3.2 Differentiation with respect to tensor arguments

Another important aspect of hyper-dual numbers is differentiation with respect to first- and second-order tensors, which will be elaborated in this section. In doing so, we

Table 3 Algebra of hyper-dual numbers

$\bar{a} + \bar{b}$	$[a_0 + b_0] + [a_1 + b_1]\epsilon_1 + [a_2 + b_2]\epsilon_2 + [a_{12} + b_{12}]\epsilon_{12}$
\overline{ab}	$[a_0b_0] + [a_0b_1 + a_1b_0]\epsilon_1 + [a_0b_2 + a_2b_0]\epsilon_2 + [a_0b_{12} + a_1b_2 + a_{12}b_0 + a_2b_1]\epsilon_{12}$
$\alpha\bar{a}$	$\alpha a_0 + \alpha a_1\epsilon_1 + \alpha a_2\epsilon_2 + \alpha a_{12}\epsilon_{12}$
$\frac{1}{\bar{a}}$	$\frac{1}{a_0} - \frac{a_1}{a_0^2}\epsilon_1 - \frac{a_2}{a_0^2}\epsilon_2 + \left[-\frac{a_{12}}{a_0^2} + \frac{2a_1a_2}{a_0^3} \right]\epsilon_{12}$
\bar{a}^n	$a_0^n + na_1a_0^{n-1}\epsilon_1 + na_2a_0^{n-1}\epsilon_2 - [na_{12}a_0^{n-1} - n[n-1]a_1a_2a_0^{n-2}]\epsilon_{12}$
$e^{\bar{a}}$	$e^{a_0} + e^{a_0}a_1\epsilon_1 + e^{a_0}a_2\epsilon_2 + e^{a_0}[a_{12} - a_1a_2]\epsilon_{12}$
$\ln(\bar{a})$	$\ln(a_0) + \frac{a_1}{a_0}\epsilon_1 + \frac{a_2}{a_0}\epsilon_2 + \left[\frac{a_{12}}{a_0} + \frac{a_1a_2}{a_0^2} \right]\epsilon_{12}$
$\sin(\bar{a})$	$\sin(a_0) + a_1 \cos(a_0)\epsilon_1 + a_2 \cos(a_0)\epsilon_2 + [a_{12} \cos(a_0) - a_1a_2 \sin(a_0)]\epsilon_{12}$
$\cos(\bar{a})$	$\cos(a_0) - a_1 \sin(a_0)\epsilon_1 - a_2 \sin(a_0)\epsilon_2 + [a_{12} \sin(a_0) + a_1a_2 \cos(a_0)]\epsilon_{12}$
$\tan(\bar{a})$	$\tan(a_0) - \frac{a_1}{\cos^2(a_0)}\epsilon_1 + \frac{a_2}{\cos^2(a_0)}\epsilon_2 + \epsilon_{12} + \left[\frac{a_{12}}{\cos^2(a_0)} + \frac{2a_1a_2 \sin(a_0)}{\cos^3(a_0)} \right]\epsilon_{12}$

provide a systematic scheme in order to define the derivatives of an arbitrary function with respect to zero-, first- and second-order functions. In order to facilitate the terminology, henceforth we refer to zero-order tensors as scalars, first-order tensors as vectors and second-order tensors simply as tensors. Also, to avoid confusing notation, we denote an independent scalar variable as z , vector variable as \mathbf{z} and tensor variable as \mathbf{Z} . Similar to classical continuum mechanics, in peridynamics the problem is associated with a potential energy function whose first and second derivatives are required in order to employ the Newton–Raphson method. Therefore, we present our framework here for scalar-valued functions with scalar, vector or tensor arguments. Such a function could represent a potential energy function. Assume ϕ is a scalar-valued function whose independent variables could be scalars $\phi(z)$, vectors $\phi(\mathbf{z})$ or tensors $\phi(\mathbf{Z})$. For the scalar variable z , using Eq. (27), the first and second derivatives of $\phi(z)$ can be obtained as

$$\begin{aligned} \frac{\partial \phi(z)}{\partial z} &= \mathfrak{S}_{\epsilon_1}(\phi(z + \epsilon_1 + \epsilon_2)) = \mathfrak{S}_{\epsilon_2}(\phi(z + \epsilon_1 + \epsilon_2)), \\ \frac{\partial^2 \phi(z)}{\partial z^2} &= \mathfrak{S}_{\epsilon_{12}}(\phi(z + \epsilon_1 + \epsilon_2)). \end{aligned} \tag{29}$$

Next, let \mathbf{a}_1 and \mathbf{a}_2 be two arbitrary vectors. Then, for the vector variable \mathbf{z} , the first and second directional derivatives of $\phi(\mathbf{z})$ in the directions \mathbf{a}_1 and \mathbf{a}_2 are calculated as

$$\begin{aligned} \frac{\partial \phi(\mathbf{z})}{\partial \mathbf{z}} \cdot \mathbf{a}_1 &= \mathfrak{S}_{\epsilon_1}(\phi(\mathbf{z} + \epsilon_1 \mathbf{a}_1)), \\ \mathbf{a}_1 \cdot \frac{\partial^2 \phi(\mathbf{z})}{\partial \mathbf{z}^2} \cdot \mathbf{a}_2 &= \mathfrak{S}_{\epsilon_{12}}(\phi(\mathbf{z} + \epsilon_1 \mathbf{a}_1 + \epsilon_2 \mathbf{a}_2)). \end{aligned} \tag{30}$$

Similarly, we assume \mathbf{A}_1 and \mathbf{A}_2 to be two arbitrary tensors. Then, for the tensor variable \mathbf{Z} , the first and second directional derivatives of $\phi(\mathbf{Z})$ in the directions \mathbf{A}_1 and \mathbf{A}_2 are

calculated as

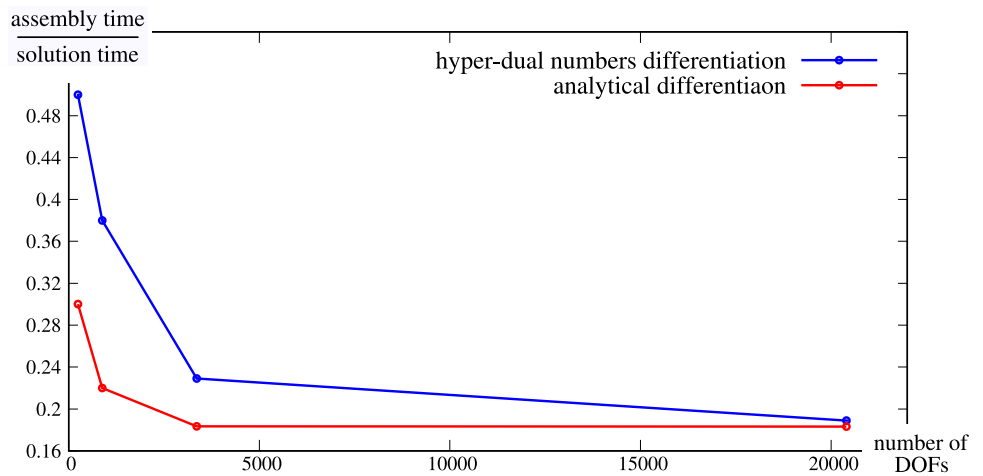
$$\begin{aligned} \frac{\partial \phi(\mathbf{Z})}{\partial \mathbf{Z}} : \mathbf{A}_1 &= \mathfrak{S}_{\epsilon_1}(\phi(\mathbf{Z} + \epsilon_1 \mathbf{A}_1)), \\ \mathbf{A}_1 : \frac{\partial^2 \phi(\mathbf{Z})}{\partial \mathbf{Z}^2} : \mathbf{A}_2 &= \mathfrak{S}_{\epsilon_{12}}(\phi(\mathbf{Z} + \epsilon_1 \mathbf{A}_1 + \epsilon_2 \mathbf{A}_2)). \end{aligned} \tag{31}$$

For further details and application of tensorial derivatives in hyperelasticity see [48, 49].

3.3 Comments on computational efficiency

The computational efficiency in derivative calculation between available methods is ranked sequentially as: analytical methods, finite difference method, complex numbers method, dual numbers method and hyper-dual numbers method, respectively [48, 49, 69]. However, the gap between the performance of methods decreases as the number of degrees of freedom in the problem increases. This is due to the fact that instead of the derivative calculation and assembly procedure, it is the solution time (inverse computation) that dominates in the computational efficiency. Figure 3 compares the computational effort required when differentiation is carried out using hyper-dual numbers (blue line) versus analytical method (red line) for our implementation. The vertical axis represents the ratio of the assembly time over the solution time and horizontal axis represents the number of DOFs. It is observed that as the number of degrees of freedom increases, the computational effort gap between the analytical scheme and hyper-dual numbers decreases. As shown in Table 3, it is observed that the summation of two hyper-dual numbers requires four real summations. Also, multiplication of two hyper-dual numbers require nine real multiplications plus five real summations. Such extended algebraic calculations are the main sources of computational cost associated with hyper-dual numbers. For example, the calculation of

Fig. 3 Comparison of the computational time when differentiating using hyper-dual numbers versus analytical differentiation. The vertical axis represents the ratio of the assembly time over the solution time and horizontal axis represents the number of DOFs



the Hessian using hyper-dual numbers is 2.5 times slower than the central difference method and 5 times slower than the forward difference method [41]. However, via adopting a mixed approach, the differentiation efficiency using hyper-dual numbers can be significantly improved in case of iterative methods such as the Newton–Raphson method. That is, instead of obtaining the convergence using hyper-dual numbers, the convergence can be obtained using real numbers and then the derivatives can be calculated via a single step hyper-dual evaluation. Such a strategy could lead the hyper-dual differentiation to be even more robust than the finite difference schemes, see [41, 43] for further details.

4 CPD with hyper-dual numbers

The final step to complete our proposed generic computational framework is to calculate the derivatives required for residual and tangents. In doing so, we carry out the differentiations using hyper-dual numbers. This strategy has three main advantages; it is compact, exact and model-independent. Thus, as the framework is implemented, any other material model can be incorporated via modifying the potential energy function solely. As mentioned before, there exist three interaction potential energy densities as

$$\begin{aligned}
 \psi_1^{ai} &= \psi_1^{ai}(|\xi^{ai}|), \\
 \psi_2^{aij} &= \psi_2^{aij}(|\mathbf{a}^{aij}|), \\
 \psi_3^{aijk} &= \psi_3^{aijk}(v^{aijk}),
 \end{aligned}
 \tag{32}$$

associated with one-, two- and three-neighbor interactions. All the potential energies are scalar-valued functions. The first two potential energies have vectors as their argument and the third potential energy has a scalar argument. Note, Eq. (32) is a more specific form of Eq. (10). All the derivations in this section are expressed in index notation. To begin, we

rewrite the three relative deformation measures as

$$\begin{aligned}
 [\xi^{ai}]_m &:= [\mathbf{x}^i]_m - [\mathbf{x}^a]_m, \\
 [\mathbf{a}^{aij}]_m &:= [\xi^{ai}]_n [\xi^{aj}]_r \mathbb{E}_{nrm}, \\
 v^{aijk} &:= [\xi^{ai}]_n [\xi^{aj}]_r [\xi^{ak}]_m \mathbb{E}_{nrm}.
 \end{aligned}
 \tag{33}$$

Similarly, for the residual we have

$$\begin{aligned}
 [\mathbf{R}_1^a]_m &= \sum_{i=1}^{\#\mathcal{N}} \left[\frac{\partial \psi_1^{ai}}{\partial \xi^{ai}} \right]_m \mathcal{V}^i, \\
 [\mathbf{R}_2^a]_m &= \sum_{i=1}^{\#\mathcal{N}} \sum_{\substack{j=1 \\ j \neq i}}^{\#\mathcal{N}} \left[2 [\xi^{aj}]_s \left[\frac{\partial \psi_2^{aij}}{\partial \mathbf{a}^{aij}} \right]_r \mathbb{E}_{srm} \right] \mathcal{V}^{ij}, \\
 [\mathbf{R}_3^a]_m &= \sum_{i=1}^{\#\mathcal{N}} \sum_{\substack{j=1 \\ j \neq i}}^{\#\mathcal{N}} \sum_{\substack{k=1 \\ k \neq i, k \neq j}}^{\#\mathcal{N}} \left[3 [\xi^{aj}]_s [\xi^{ak}]_r \left[\frac{\partial \psi_3^{aijk}}{\partial v^{aijk}} \right] \mathbb{E}_{srm} \right] \mathcal{V}^{ijk},
 \end{aligned}
 \tag{34}$$

for which the first derivatives of the potential energy with respect to the relative deformation measures are required. Using the formulation presented in Eqs. (29) and (30) we have

$$\begin{aligned}
 \left[\frac{\partial \psi_1^{ai}}{\partial \xi^{ai}} \right]_m &= \mathfrak{S}_{\epsilon_1} \left(\psi_1^{ai}(\xi^{ai} + \epsilon_1 \mathbf{e}_m) \right) \\
 &= \mathfrak{S}_{\epsilon_2} \left(\psi_1^{ai}(\xi_m^{ai} + \epsilon_1 \mathbf{e}_m) \right), \\
 \left[\frac{\partial \psi_2^{aij}}{\partial \mathbf{a}^{aij}} \right]_m &= \mathfrak{S}_{\epsilon_1} \left(\psi_2^{aij}(\mathbf{a}_m^{aij} + \epsilon_1 \mathbf{e}_m) \right) \\
 &= \mathfrak{S}_{\epsilon_2} \left(\psi_2^{aij}(\mathbf{a}_m^{aij} + \epsilon_1 \mathbf{e}_m) \right),
 \end{aligned}$$

$$\begin{aligned} \left[\frac{\partial \psi_3^{ajk}}{\partial v^{ajk}} \right] &= \mathfrak{S}_{\epsilon_1} \left(\psi_3^{ajk} (v^{ajk} + \epsilon_1) \right) \\ &= \mathfrak{S}_{\epsilon_2} \left(\psi_3^{ajk} (v^{ajk} + \epsilon_1) \right), \end{aligned} \tag{35}$$

with \mathbf{e}_m being the unit vector in the m th coordinate direction. To proceed with the calculation of tangents, we rewrite Eq. (20) in index notation as

$$\begin{aligned} [\mathbf{K}_1^{ab}]_{mn} &= \left[\frac{\partial \mathbf{R}_1^a}{\partial \mathbf{x}^b} \right]_{mn} \\ &= \left[\frac{\partial}{\partial \mathbf{x}^b} \right]_n \left(\sum_{i=1}^{\#\mathcal{N}} \left[\frac{\partial \psi_1^{ai}}{\partial \xi^{ai}} \right]_m \mathcal{V}^i \right), \\ [\mathbf{K}_2^{ab}]_{mn} &= \left[\frac{\partial \mathbf{R}_2^a}{\partial \mathbf{x}^b} \right]_{mn} = \left[\frac{\partial}{\partial \mathbf{x}^b} \right]_n \\ &\quad \left(\sum_{i=1}^{\#\mathcal{N}} \sum_{\substack{j=1 \\ j \neq i}}^{\#\mathcal{N}} 2 [\xi^{aj}]_s \left[\frac{\partial \psi_2^{aj}}{\partial \mathbf{a}^{aj}} \right]_r \mathbb{e}_{srm} \mathcal{V}^{ij} \right), \\ [\mathbf{K}_3^{ab}]_{mn} &= \left[\frac{\partial \mathbf{R}_3^a}{\partial \mathbf{x}^b} \right]_{mn} = \left[\frac{\partial}{\partial \mathbf{x}^b} \right]_n \\ &\quad \left(\sum_{i=1}^{\#\mathcal{N}} \sum_{\substack{j=1 \\ j \neq i}}^{\#\mathcal{N}} \sum_{\substack{k=1 \\ k \neq j}}^{\#\mathcal{N}} 3 [\xi^{aj}]_s [\xi^{ak}]_r \left[\frac{\partial \psi_3^{ajk}}{\partial v^{ajk}} \right] \mathbb{e}_{srm} \mathcal{V}^{ijk} \right). \end{aligned} \tag{36}$$

Moreover, to use the chain rule, the following constitutive model-independent, geometric relations prove to be useful

$$\begin{aligned} \left[\frac{\partial \xi^{ai}}{\partial \mathbf{x}^b} \right]_{mn} &= [\delta^{ib} - \delta^{ab}] \delta_{mn}, \\ \left[\frac{\partial \mathbf{a}^{aj}}{\partial \mathbf{x}^b} \right]_{mn} &= \left[\frac{\partial [\xi^{ai} \times \xi^{aj}]}{\partial \mathbf{x}^b} \right]_{mn} \\ &= \left[[\delta^{ib} - \delta^{ab}] [\xi^{aj}]_s \right. \\ &\quad \left. - [\delta^{jb} - \delta^{ab}] [\xi^{ai}]_s \right] \mathbb{e}_{mns}, \\ \left[\frac{\partial v^{ajk}}{\partial \mathbf{x}^b} \right]_m &= \left[\frac{\partial [\xi^{ai} \cdot [\xi^{aj} \times \xi^{ak}]]}{\partial \mathbf{x}^b} \right]_m \\ &= \left[[\delta^{ib} - \delta^{ab}] [\xi^{aj}]_n [\xi^{ak}]_s \right. \\ &\quad + [\delta^{jb} - \delta^{ab}] [\xi^{ak}]_n [\xi^{ai}]_s \\ &\quad \left. + [\delta^{kb} - \delta^{ab}] [\xi^{ai}]_n [\xi^{aj}]_s \right] \mathbb{e}_{mns}. \end{aligned} \tag{37}$$

for the details on the derivations, see Appendix B. Accordingly, using relations in Eq. (37), the final form of the tangents read

$$\begin{aligned} [\mathbf{K}_1^{ab}]_{mn} &= \sum_{i=1}^{\#\mathcal{N}} \left[[\delta^{ib} - \delta^{ab}] \left[\frac{\partial^2 \psi_1^{ai}}{\partial \xi^{ai^2}} \right]_{mn} \right] \mathcal{V}^i, \\ [\mathbf{K}_2^{ab}]_{mn} &= \sum_{i=1}^{\#\mathcal{N}} \sum_{\substack{j=1 \\ j \neq i}}^{\#\mathcal{N}} \\ &\quad \left[2 [\delta^{jb} - \delta^{ab}] \left[\frac{\partial \psi_2^{aj}}{\partial \mathbf{a}^{aj}} \right]_r \mathbb{e}_{nrm} + 2 [\xi^{aj}]_s \right. \\ &\quad \left[[\delta^{ib} - \delta^{ab}] [\xi^{aj}]_t - [\delta^{jb} - \delta^{ab}] [\xi^{ai}]_t \right] \\ &\quad \left. \left[\frac{\partial^2 \psi_2^{aj}}{\partial \mathbf{a}^{aj^2}} \right]_{rq} \mathbb{e}_{qnt} \mathbb{e}_{srm} \right] \mathcal{V}^{ij}, \\ [\mathbf{K}_3^{ab}]_{mn} &= \sum_{i=1}^{\#\mathcal{N}} \sum_{\substack{j=1 \\ j \neq i}}^{\#\mathcal{N}} \sum_{\substack{k=1 \\ k \neq j}}^{\#\mathcal{N}} \\ &\quad \left[3 [\delta^{jb} - \delta^{ab}] [\xi^{ak}]_r - [\delta^{kb} - \delta^{ab}] [\xi^{aj}]_r \right] \\ &\quad \left[\frac{\partial \psi_3^{ajk}}{\partial v^{ajk}} \right]_{mnr} + 3 [\xi^{aj}]_s [\xi^{ak}]_r \\ &\quad \left[[\delta^{ib} - \delta^{ab}] [\xi^{aj}]_q [\xi^{ak}]_t \right. \\ &\quad \left. + [\delta^{jb} - \delta^{ab}] [\xi^{ak}]_q [\xi^{ai}]_t \right. \\ &\quad \left. + [\delta^{kb} - \delta^{ab}] [\xi^{ai}]_q [\xi^{aj}]_t \right] \\ &\quad \left. \left[\frac{\partial^2 \psi_3^{ajk}}{\partial v^{ajk^2}} \right]_{msr} \mathbb{e}_{nqt} \right] \mathcal{V}^{ijk}. \end{aligned} \tag{38}$$

The last step to determine the tangents is to calculate the second derivatives of the potential energy with respect to the relative deformation measures. Using the formulations presented in Eqs. (29)–(31) we have

$$\begin{aligned} \left[\frac{\partial^2 \psi_1^{ai}}{\partial \xi^{ai^2}} \right]_{mn} &= \mathfrak{S}_{\epsilon_{12}} \left(\psi_1^{ai} (\xi^{ai} + \epsilon_1 [\mathbf{e}_m \otimes \mathbf{e}_n] + \epsilon_2 [\mathbf{e}_m \otimes \mathbf{e}_n]) \right), \\ \left[\frac{\partial^2 \psi_2^{aj}}{\partial \mathbf{a}^{aj^2}} \right]_{mn} &= \mathfrak{S}_{\epsilon_{12}} \left(\psi_2^{aj} (\mathbf{a}_m^{aj} + \epsilon_1 [\mathbf{e}_m \otimes \mathbf{e}_n] + \epsilon_2 [\mathbf{e}_m \otimes \mathbf{e}_n]) \right), \\ \left[\frac{\partial^2 \psi_3^{ajk}}{\partial v^{ajk^2}} \right] &= \mathfrak{S}_{\epsilon_{12}} \left(\psi_3^{ajk} (v^{ajk} + \epsilon_1 + \epsilon_2) \right). \end{aligned} \tag{39}$$

Fig. 4 Illustration of the behavior of the functions S_1 and ψ_1^{ai} with respect to λ_ξ for different values of n . For the bottom plot, it is assumed $C_1 = 1$ and $|\Xi^{ai}| = 1$. Similar behavior can be observed for the pair S_2 and ψ_2^{aij} and the pair S_3 and ψ_3^{aijk}

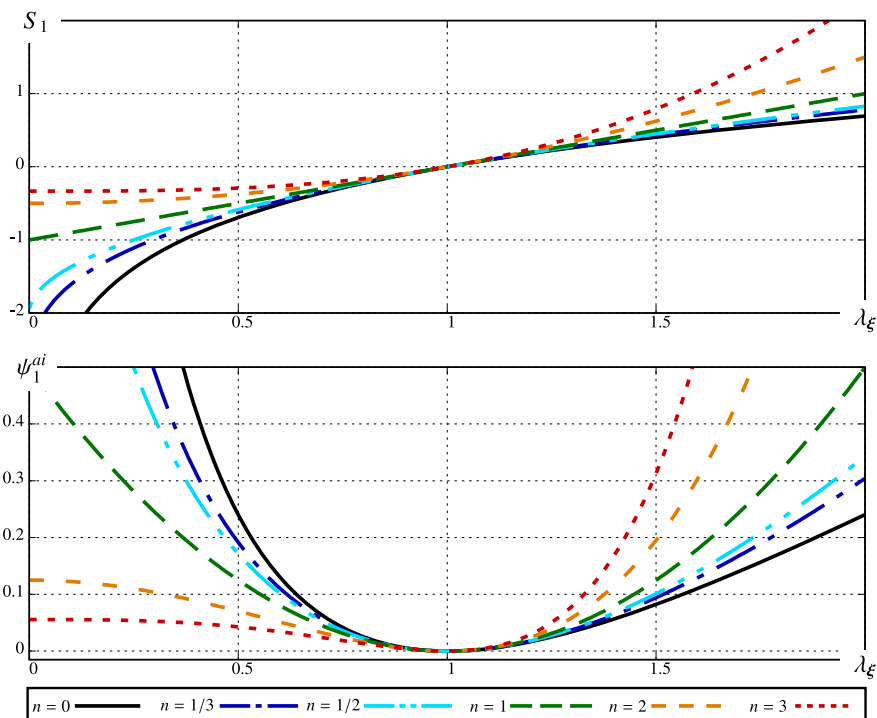


Table 4 Convergence behavior associated with the right set in Fig. 5 with $C_2/C_1 \gg 1$ at different deformations. The top segment corresponds to the case with differentiation with hyper-dual numbers and the bottom segment corresponds to the case with analytical differentiations

$\frac{\ \mathbb{R}\ }{\ \mathbb{R}_1\ }$	iteration	20% deformation	40% deformation	60% deformation	80% deformation	100% deformation
differentiation with hyper-dual numbers	1	1.00E+00	1.00E+00	1.00E+00	1.00E+00	1.00E+00
	2	3.53E-02	4.41E-02	7.97E-02	9.18E-02	1.10E-01
	3	1.31E-03	5.46E-03	8.84E-03	2.64E-02	2.95E-02
	4	2.30E-06	1.87E-05	4.87E-03	7.89E-03	6.46E-03
	5	5.87E-12	2.80E-10	7.90E-06	1.29E-05	5.93E-06
	6	3.15E-14	3.62E-14	5.42E-11	1.58E-10	1.97E-11
differentiation with analytical derivatives	1	1.00E+00	1.00E+00	1.00E+00	1.00E+00	1.00E+00
	2	3.53E-02	4.41E-02	7.97E-02	9.18E-02	1.10E-01
	3	1.31E-03	5.46E-03	8.84E-03	2.64E-02	2.95E-02
	4	2.30E-06	1.87E-05	4.87E-03	7.89E-03	6.46E-03
	5	5.87E-12	2.80E-10	7.90E-06	1.29E-05	5.93E-06
	6	3.13E-14	3.61E-14	5.42E-11	1.58E-10	1.97E-11

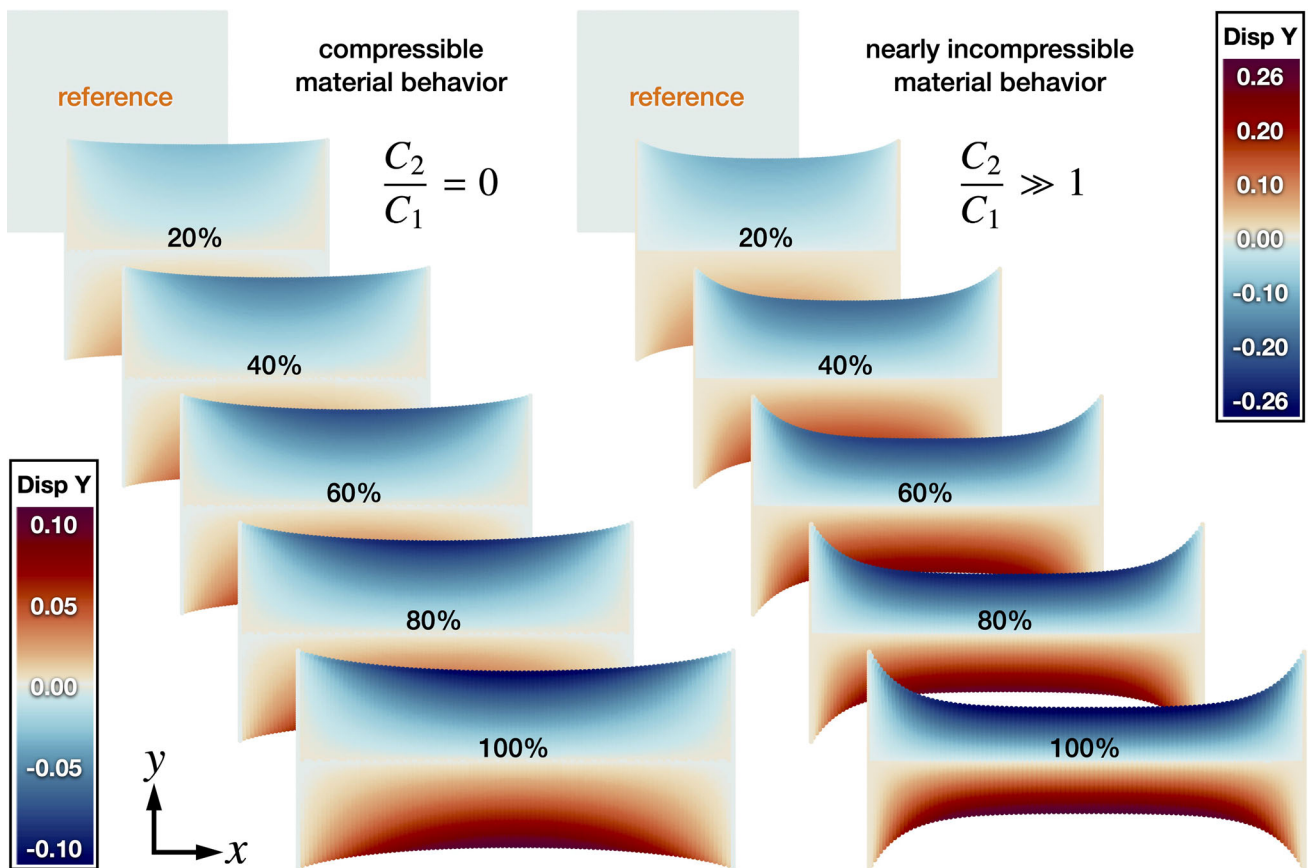


Fig. 5 Deformation of a unit square undergoing 100% extension in compressible and nearly compressible regimes. The left set corresponds to the compressible material behavior with the ratio $C_2/C_1 = 0$ and the right set corresponds to the nearly incompressible material behavior with the ratio $C_2/C_1 \gg 1$

As mentioned earlier, the main advantage of our proposed framework is that it is model-independent. That is, once it is implemented, any other material model can be incorporated via modifying the potential energy function solely.

5 Internal potential energy

The last step to complete our proposed framework is to define an internal energy potential. In this manuscript, we define a family of internal potential energies based on the Seth–Hill strain measures. To proceed, it proves convenient to define scalar-valued ratios of the deformation measures in CPD as

$$\begin{aligned} \lambda_\xi &= \frac{|\xi^{ai}|}{|\mathbf{E}^{ai}|}, \\ \lambda_a &= \frac{|a^{aij}|}{|A^{aij}|}, \\ \lambda_v &= \frac{v^{aijk}}{V^{aijk}}. \end{aligned} \quad (40)$$

As mentioned before, the internal potential energy consists of the contribution of one-, two- and three-neighbor interactions. Accordingly we define the discretized energies as

$$\begin{aligned} \psi_1^{ai} &= \frac{1}{2} C_1 |\mathbf{E}^{ai}| S_1^2, \\ \psi_2^{aij} &= \frac{1}{2} C_2 |A^{aij}| S_2^2, \\ \psi_3^{aijk} &= \frac{1}{2} C_3 V^{aijk} S_3^2, \end{aligned} \quad (41)$$

with the sufficient but not necessary conditions $C_1 > 0$, $C_2 \geq 0$ and $C_3 \geq 0$ to guarantee positiveness of the energy, where

$$\begin{aligned} S_1 &= \begin{cases} \frac{1}{n} [\lambda_\xi^n - 1] & n \neq 0, \\ \ln \lambda_\xi & n = 0, \end{cases} \\ S_2 &= \begin{cases} \frac{1}{n} [\lambda_a^n - 1] & n \neq 0, \\ \ln \lambda_a & n = 0, \end{cases} \end{aligned}$$

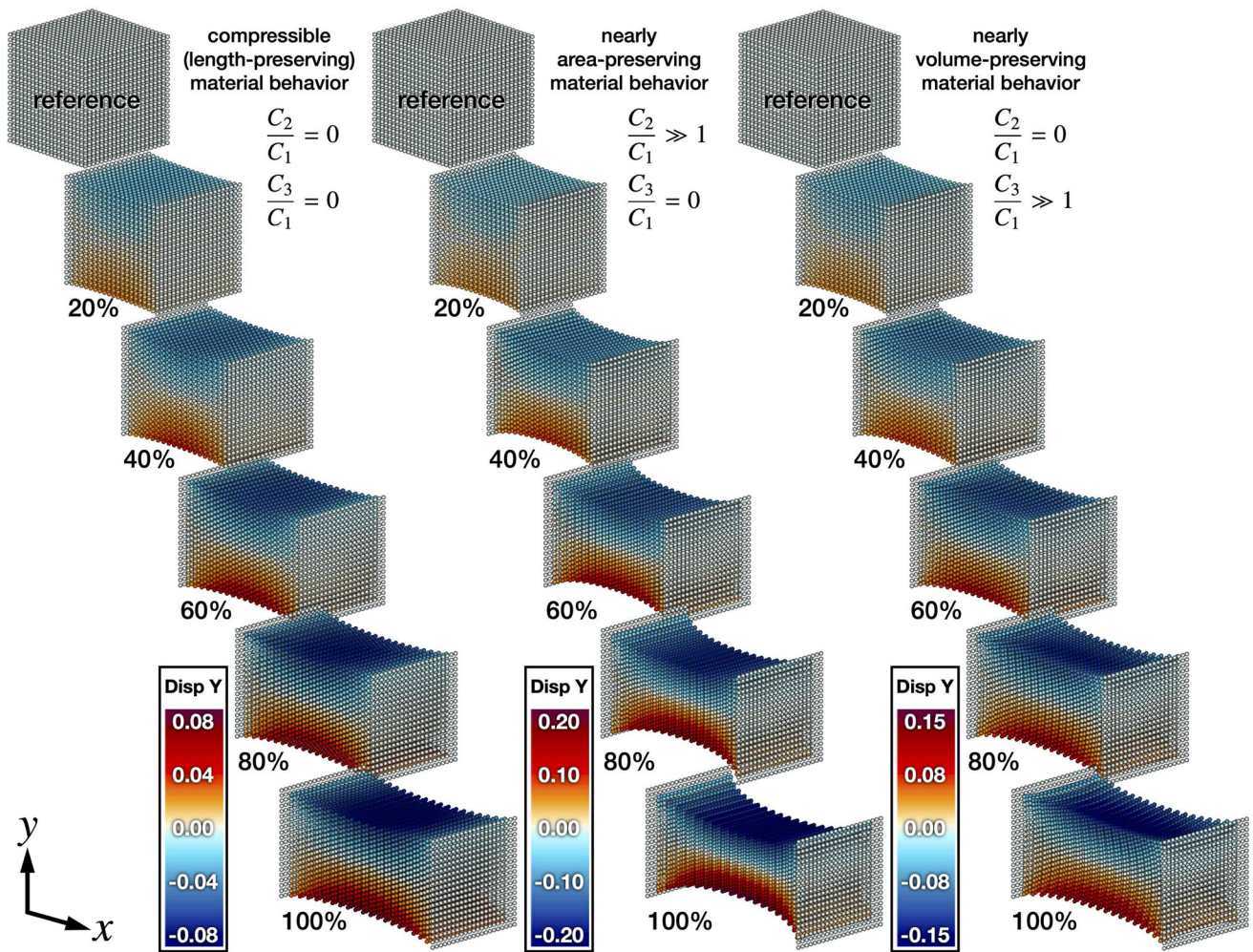


Fig. 6 Deformation of a unit cube undergoing 100% extension in for three different material behaviors. The left set corresponds to the compressible or length-preserving material behavior with the ratios $C_2/C_1 = 0$ and $C_3/C_1 = 0$. The middle set corresponds to the

area-preserving material behavior with the ratios $C_2/C_1 \gg 1$ and $C_3/C_1 = 0$. The right set corresponds to the volume-preserving material behavior with the ratios $C_2/C_1 = 0$ and $C_3/C_1 \gg 1$

$$S_3 = \begin{cases} \frac{1}{n} [\lambda_v^n - 1] & n \neq 0, \\ \ln \lambda_v & n = 0, \end{cases} \quad (42)$$

Figure 4 illustrates the behavior of the functions S_1 and ψ_1^{ai} with respect to λ_ξ for different values of n . Note, for the potential energy (bottom plot) we assume $C_1 = 1$ and $|\Xi^{ai}| = 1$. For $\lambda_\xi < 1$, smaller values of n render higher energy potentials whereas for $\lambda_\xi > 1$ the opposite behavior is observed.

6 Numerical examples

The objective of this section is to illustrates the performance of our proposed computational framework enabled by hyper-dual numbers. In doing so, three different studies are

carried out with different combinations of the internal potential energies introduced in Eqs. (41) and (42). Our simulations demonstrate the influence of multi-neighbor interactions on the material response together with the robustness of the framework and its consistent quadratic convergence even at very large deformations. All the examples are solved using our in-house CPD code written in C++.

6.1 Uniaxial tension

The objective of this study is to evaluate the accuracy of the computations using hyper-dual numbers. In doing so, a unit specimen is subject to 100% uniaxial tension and the convergence behaviors due to analytical derivatives and hyper-dual numbers derivatives are compared. Figure 5 illustrates a 2D analysis where two different material behaviors

Table 5 Convergence behavior associated with the left set in Fig. 5 with $C_2/C_1 = 0$ at different deformations. The top segment corresponds to the case with differentiation with hyper-dual numbers and the bottom segment corresponds to the case with analytical differentiations

$\frac{\ \mathbb{R}\ }{\ \mathbb{R}_1\ }$	iteration	20% deformation	40% deformation	60% deformation	80% deformation	100% deformation
differentiation with hyper-dual numbers	1	1.00E+00	1.00E+00	1.00E+00	1.00E+00	1.00E+00
	2	6.19E-02	4.85E-02	3.82E-02	3.04E-02	2.45E-02
	3	5.20E-04	2.35E-04	1.12E-04	5.82E-05	3.28E-05
	4	4.28E-08	7.27E-09	1.60E-09	4.53E-10	1.50E-10
	5	2.60E-14	3.22E-14	3.61E-14	3.92E-14	4.13E-14
	6	2.61E-14	3.22E-14	3.62E-14	3.91E-14	4.14E-14
differentiation with analytical derivatives	1	1.00E+00	1.00E+00	1.00E+00	1.00E+00	1.00E+00
	2	6.19E-02	4.85E-02	3.82E-02	3.04E-02	2.45E-02
	3	5.20E-04	2.35E-04	1.12E-04	5.82E-05	3.28E-05
	4	4.28E-08	7.27E-09	1.60E-09	4.53E-10	1.50E-10
	5	2.37E-14	2.69E-14	2.88E-14	3.11E-14	3.22E-14
	6	2.37E-14	2.70E-14	2.89E-14	3.11E-14	3.22E-14

are considered. The left column corresponds to a compressible material behavior where $C_2/C_1 = 0$ and the right column corresponds to the case with nearly incompressible material behavior where $C_2/C_1 \gg 1$.² The grid spacing for both cases is $\Delta = 0.01$ and the ratio of the horizon size over grid spacing is $\delta/\Delta = 3$. For this study, we consider the potential energy introduced in Eqs. (41) and (42) with $n = 1$. Thus, $S_1 = [\lambda_\xi - 1]$, $S_2 = [\lambda_a - 1]$ and $S_3 = [\lambda_v - 1]$. The undeformed configurations are depicted at the top and the deformed configurations at the intermediate steps are shown subsequently. The vertical displacement distribution is shown throughout each specimen. It is observed that the case with $C_2/C_1 \gg 1$ renders more lateral contraction compared to the case with $C_2/C_1 = 0$ which is justifiable since larger values of C_2/C_1 indicate more incompressibility. Table 5 compares the convergence behavior associated with Fig. 5-left for the compressible material behavior. The top segment corresponds to the case where the differentiation is carried out using hyper-dual numbers and the bottom segment corresponds to the case where the differentiation is calculated analytically. Columns correspond to different deformation magnitudes whereas rows show the normalized L_2 -norm of the residual at each Newton–Raphson iteration. A quadratic convergence rate is observed for both

cases which is expected due to the use of Newton–Raphson scheme. The convergence due to hyper-dual numbers is identical to the one obtained by analytical derivations for the first few steps. Minor differences are observed at the last steps which originate from machine precision induced round-off. Table 4 is the counter part of Table 5 for the nearly incompressible material behavior associated with Fig. 5-right. Similar to the previous case, an identical trend is observed for the convergence due to the hyper-dual numbers and the analytical derivatives.

Figure 6 illustrates a 3D analysis where a unit cube is subject to 100% uniaxial tension. The grid spacing for this study is $\Delta = 0.05$ and the ratio of the horizon size over grid spacing is $\delta/\Delta = 3$. Three different types of interactions are considered for this example. One-neighbor interactions with $C_2/C_1 = 0$ and $C_3/C_1 = 0$ render compressible or length-preserving material behavior, one- and two-neighbor interactions with $C_2/C_1 \gg 1$ and $C_3/C_1 = 0$ render nearly area-preserving behavior, and one- and three-neighbor interactions with $C_2/C_1 \gg 1$ and $C_3/C_1 \gg 1$ rendering volume-preserving behavior³. As demonstrated in [13], we emphasize that it is not possible to have only two-neighbor interactions or only three-neighbor interactions. When only one neighbor interactions are taken into account, the least

² The relation $C_2/C_1 \gg 1$ in CPD is our way of expressing incompressibility. The actual values of the material parameters for this case is $C_1 = 2.8266 \times 10^6$ and $C_2 = 2.8973 \times 10^{12}$.

³ The relation $C_3/C_1 \gg 1$ in CPD is our way of expressing incompressibility. The actual values of the material parameters for this case is $C_1 = 1.83 \times 10^5$ and $C_2 = 1.21 \times 10^{12}$.

Table 6 Convergence behavior associated with the left set in Fig. 6 with $C_2/C_1 = 0$ and $C_3/C_1 = 0$ at different deformations. The top segment corresponds to the case with differentiation with hyper-dual

numbers and the bottom segment corresponds to the case with analytical differentiations

$\frac{\ \mathbb{R}\ }{\ \mathbb{R}_1\ }$	iteration	20% deformation	40% deformation	60% deformation	80% deformation	100% deformation
differentiation with hyper-dual numbers	1	1.00E+00	1.00E+00	1.00E+00	1.00E+00	1.00E+00
	2	3.99E-02	2.87E-02	2.08E-02	1.54E-02	1.15E-02
	3	7.66E-05	2.90E-05	1.16E-05	5.08E-06	2.41E-06
	4	3.79E-10	4.56E-11	6.64E-12	1.18E-12	2.51E-13
	5	2.52E-14	3.61E-14	4.32E-14	4.85E-14	5.26E-14
	6	2.52E-14	3.60E-14	4.32E-14	4.85E-14	5.26E-14
differentiation with analytical derivatives	1	1.00E+00	1.00E+00	1.00E+00	1.00E+00	1.00E+00
	2	3.99E-02	2.87E-02	2.08E-02	1.54E-02	1.15E-02
	3	7.66E-05	2.90E-05	1.16E-05	5.08E-06	2.41E-06
	4	3.79E-10	4.56E-11	6.64E-12	1.18E-12	2.47E-13
	5	1.25E-14	1.40E-14	1.44E-14	1.61E-14	1.68E-14
	6	1.26E-14	1.38E-14	1.45E-14	1.61E-14	1.68E-14

Table 7 Convergence behavior associated with the middle set in Fig. 6 with $C_2/C_1 \gg 1$ and $C_3/C_1 = 0$ at different deformations. The top segment corresponds to the case with differentiation with hyper-dual

numbers and the bottom segment corresponds to the case with analytical differentiations

$\frac{\ \mathbb{R}\ }{\ \mathbb{R}_1\ }$	iteration	20% deformation	40% deformation	60% deformation	80% deformation	100% deformation
differentiation with hyper-dual numbers	1	1.00E+00	1.00E+00	1.00E+00	1.00E+00	1.00E+00
	2	3.60E-02	3.18E-02	2.82E-02	2.56E-02	2.37E-02
	3	1.18E-04	8.75E-05	6.27E-05	4.59E-05	3.52E-05
	4	2.36E-09	1.08E-09	4.86E-10	2.43E-10	1.41E-10
	5	1.06E-13	1.63E-13	2.14E-13	2.55E-13	2.91E-13
	6	1.06E-13	1.63E-13	2.14E-13	2.55E-13	2.91E-13
differentiation with analytical derivatives	1	1.00E+00	1.00E+00	1.00E+00	1.00E+00	1.00E+00
	2	3.65E-02	3.18E-02	2.82E-02	2.56E-02	2.37E-02
	3	1.22E-04	8.75E-05	6.27E-05	4.59E-05	3.52E-05
	4	2.58E-09	1.08E-09	4.86E-10	2.43E-10	1.41E-10
	5	1.29E-14	1.59E-14	1.76E-14	1.79E-14	1.93E-14
	6	1.28E-14	1.59E-14	1.73E-14	1.76E-14	1.88E-14

Table 8 Convergence behavior associated with the right set in Fig. 6 with $C_2/C_1 = 0$ and $C_3/C_1 \gg 1$ at different deformations. The top segment corresponds to the case with differentiation with hyper-dual

numbers and the bottom segment corresponds to the case with analytical differentiations

$\frac{\ \mathbb{R}\ }{\ \mathbb{R}_1\ }$	iteration	20% deformation	40% deformation	60% deformation	80% deformation	100% deformation
differentiation with hyper-dual numbers	1	1.00E+00	1.00E+00	1.00E+00	1.00E+00	1.00E+00
	2	3.37E-02	2.85E-02	2.42E-02	2.10E-02	1.85E-02
	3	1.04E-04	6.12E-05	3.64E-05	2.25E-05	1.47E-05
	4	1.60E-09	4.29E-10	1.29E-10	4.47E-11	1.81E-11
	5	1.88E-14	2.70E-14	3.27E-14	3.76E-14	4.11E-14
	6	1.89E-14	2.69E-14	3.26E-14	3.77E-14	4.11E-14
differentiation with analytical derivatives	1	1.00E+00	1.00E+00	1.00E+00	1.00E+00	1.00E+00
	2	3.37E-02	2.85E-02	2.42E-02	2.10E-02	1.85E-02
	3	1.04E-04	6.12E-05	3.64E-05	2.25E-05	1.47E-05
	4	1.60E-09	4.29E-10	1.29E-10	4.47E-11	1.81E-11
	5	1.44E-14	1.82E-14	2.10E-14	2.53E-14	3.01E-14
	6	1.40E-14	1.71E-14	1.83E-14	2.07E-14	2.26E-14

contraction is obtained which leads to increased compressibility. More incompressibility is observed when one- and two-neighbor interactions or one- and three-neighbor interactions are considered. It is important to note that although accounting for both two-neighbor interactions and three-neighbor interactions result in decreased compressibility, the solutions are different indicating that they indeed correspond to a different deformations. Tables 6, 7, 8 exhibit the convergence behavior for the three material behaviors in Fig. 6. Similarly, the residual obtained via hyper-dual number differentiation and analytical differentiation are almost identical where only minor differences are observed at the very last steps.

6.2 Bending

In this study we exhibit the capability of CPD to tackle with problems involving large deformations. In doing so, a cantilever beam is subject to rotation and compression at its free end as shown in Fig. 7. The top row corresponds to a 3D analysis and the bottom row corresponds to a 2D analysis. For both cases, the grid spacing for this study is $\Delta = 0.02$ and the ratio of the horizon size over grid spacing is $\delta/\Delta = 3$. The material constants in this example are $C_1 = 1$ and $C_2 = 10^4$. The colors indicate the deflection in y-direction and the intermediate deformed configurations are depicted for each case.

For this study, we consider the potential energy introduced in Eqs. (41) and (42) with $n = 2$. Thus, $S_1 = \frac{1}{2} [\lambda_\xi^2 - 1]$ and $S_2 = \frac{1}{2} [\lambda_a^2 - 1]$ For all the cases, the aspect ratio of the beam is 25 and one- and two-neighbor interactions are considered representing a compressible material response. The deformation is applied such that at each increment the points are incrementally rotated with respect to the clamped end and then are vertically compressed proportional to their initial displacement. For instance, if a point's vertical displacement due to the initial rotation is x , then after the rotation it is vertically compressed with a magnitude of ax with $0 < a < 1$. Three different values for a are considered in this study. In the left column the compression magnitude is $a = 0.1$, in the middle column the compression magnitude is $a = 0.3$ and in the right column the compression magnitude is $a = 0.5$. As the compression magnitude increases, it is observed that the beams tend to increase their curvature in order to maintain their length.

6.3 Torsion

The final example is devised to compare the robustness of our computational framework for bulk-dominated and surface-dominated geometries. Figures 8 and 9 exhibit two blocks with slenderness ratios of 2 and 4, respectively, that are subject to 180° torsion. For both cases the material constants

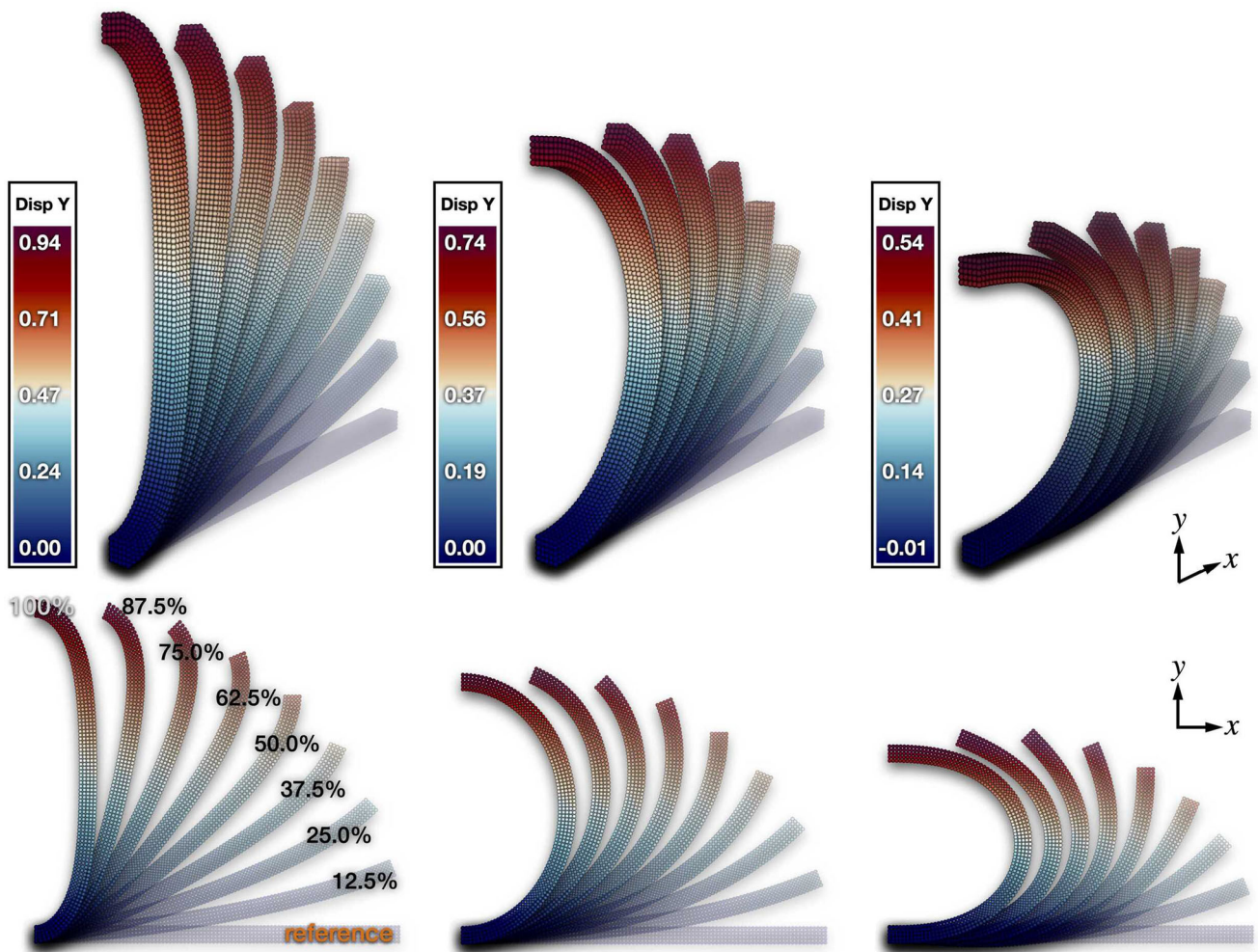


Fig. 7 Deformation of cantilever beam subject to 90° rotation and three different magnitudes of compression in 3D and 2D settings. In the left column the compression magnitude is 0.1, in the middle column the

compression magnitude is 0.3 and in the right column the compression magnitude is 0.5. Colors represent deflection in y -direction

are $C_1 = 1$, $C_2 = 0$ and $C_3 = 10^8$. The deformed bodies together with their corresponding convergence are shown at different twisting angles. The colors indicate the deflection in y -direction. For both cases, the grid spacing for this study is $\Delta = 0.02$ and the ratio of the horizon size over grid spacing is $\delta/\Delta = 3$. For this study, we consider the potential energy introduced in Eqs. (41) and (42) with $n = 0$, thus, $S_1 = \ln \lambda_\xi$ and $S_3 = \ln \lambda_\nu$. For the block with slenderness ratio 2, since the value of the horizon is small compared to the block's cross-section, the problem is more of a bulk-dominated type. On the other hand, for the block with slenderness ratio of 4, the problem is more of a surface-dominated type due to comparable values of the horizon and cross-section. Fewer steps are required to obtain the convergence for the case with larger slenderness ratio which is understandable since there are less collocations points hence less degrees of freedom. Nonethe-

less, it is observed that our computational framework can deal with large deformations without losing its robustness.

6.4 Nonlocality

Finally, as the last study, we aim to demonstrate the nonlocality of CDP. In doing so, as depicted in Fig. 10, an infinitesimal vertical displacement is applied to an L-shaped specimen and the value of the von Mises stress in the vicinity of the sharp corner highlighted in Fig. 10 is investigated in both vertical and horizontal directions. For this study, the ratio of the horizon size to grid spacing is fixed $\delta/\Delta = 3.0$ and the value of the grid spacing Δ is increased, leading to a more nonlocal behavior. This example is carried out for a compressible material behavior where $\nu = 0.33$, thus we set the material constant C_2 to zero and change C_1 in accordance with Δ in order to satisfy $\nu = 0.33$, see [18] for further details. In

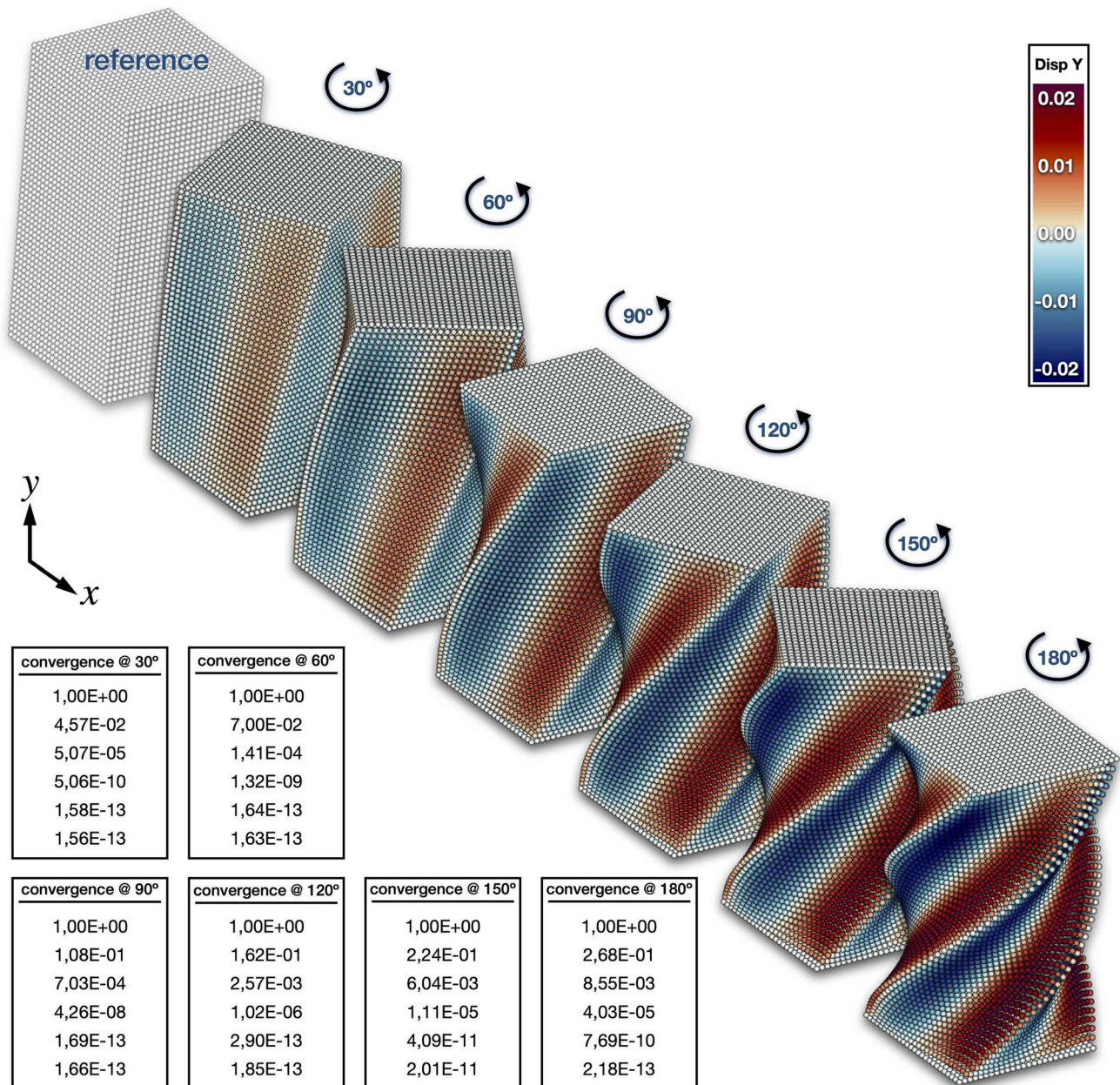


Fig. 8 Deformation of a block with slenderness ratio of 2 under 180° torsion. The deformed bodies together with their corresponding convergence are shown at different twisting angles. Colors represent deflection in y-direction

Fig. 10 left, the von Mises stress in the horizontal direction is plotted and in Fig. 10 right, the von Mises stress in the vertical direction is plotted. It is observed that as the value of grid spacing Δ increases, the stress concentration at the vicinity of the corner decreases which indicates a more nonlocal response. Similarly, the highest stress concentration occurs for the case with the most local effect which is associated with smallest Δ . Note that for this study, we consider the potential energy introduced in Eqs. (41) and (42) with $n = 1$. Thus, $S_1 = [\lambda_\xi - 1]$.

Motivated by the previous observation regarding the capability of CPD to capture nonlocal effects, our methodology can be adopted to determine the overall response materials with complex micro-structures. A well-known example of such material is brain tissue. Several studies has been carried out to determine the mechanical properties of brain tissue [71–73]. Figure 11 shows a brain sample with its cut-out which is subject to infinitesimal shear deformation. Such specimen is utilized to carry out rheometry analysis in order to determine the mechanical properties of brain matter. Undoubtedly, investigation of the nonlocal effects in brain

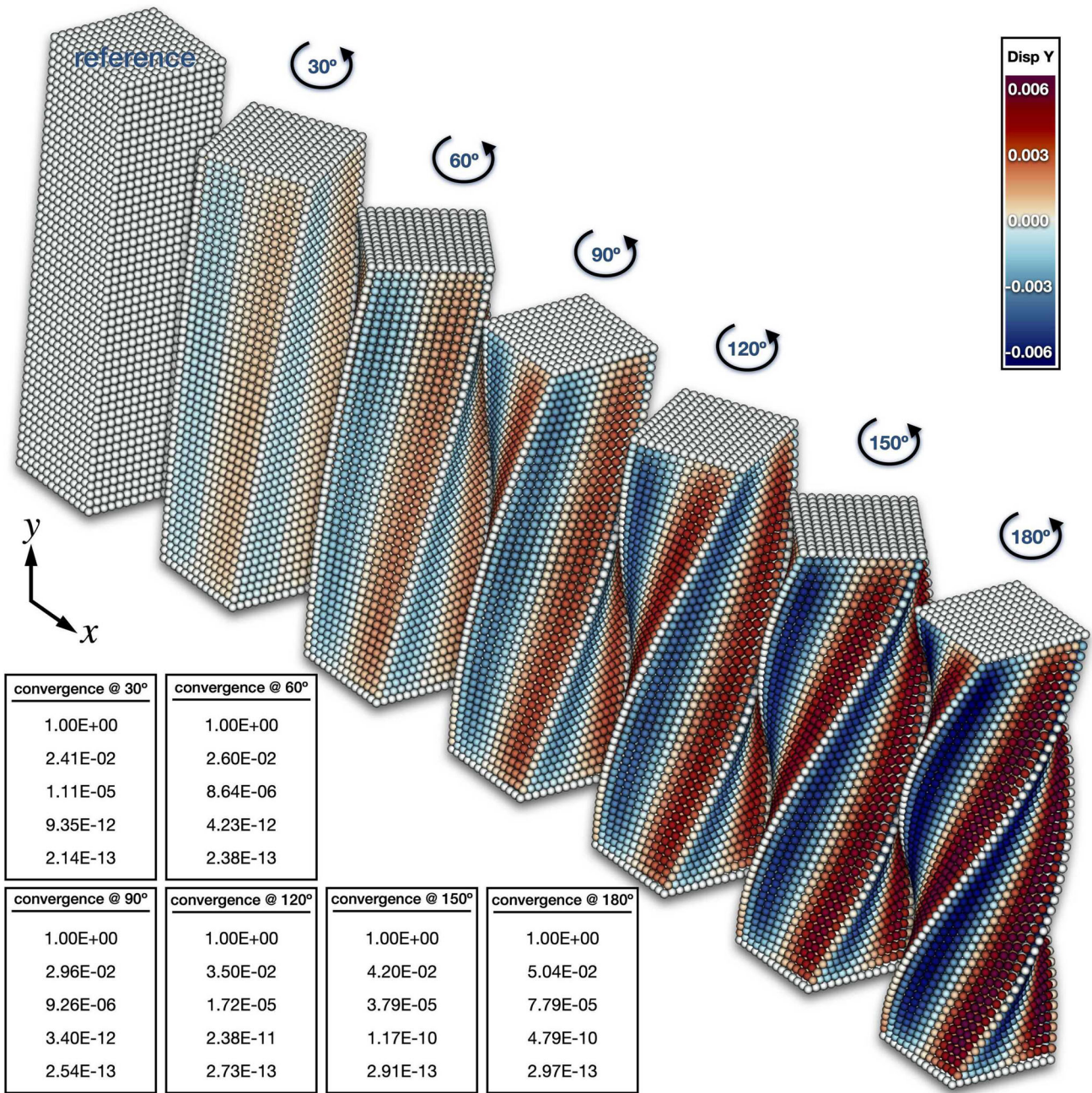


Fig. 9 Deformation of a block with slenderness ratio of 4 under 180° torsion. The deformed bodies together with their corresponding convergence are shown at different twisting angles. Colors represent deflection in y-direction

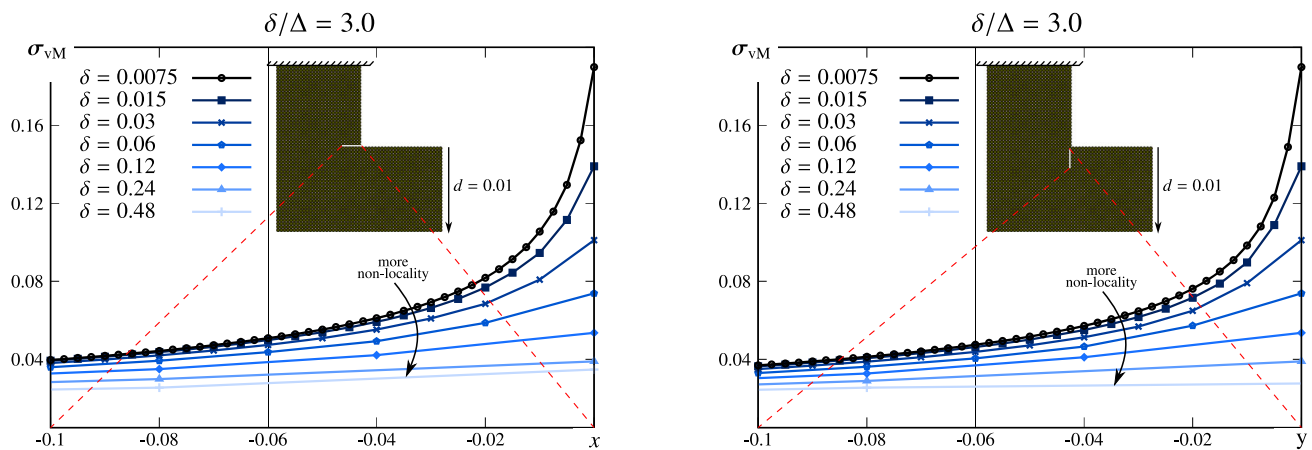


Fig. 10 CPD nonlocality study on stress concentration in an L-shaped specimen undergoing infinitesimal vertical displacement. The post-processed von Mises stress through the highlighted arrow in the domain is plotted. For the left plot, the horizon-to-lattice size ratio is fixed $\delta/\Delta = 3.0$ and the lattice size is decreased. For the right plot, the

lattice size ratio is fixed $\Delta = 0.005$ and the horizon-to-lattice size ratio is decreased. Stress-like quantities in CPD can be computed in post-processing via an integral over the horizon, similar to the customary practice in computational homogenization [70]

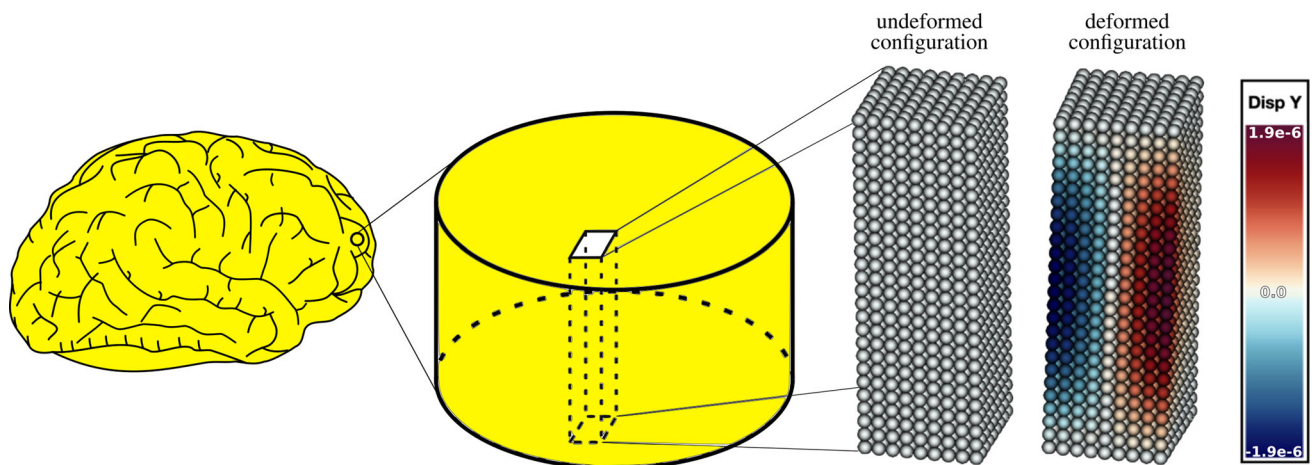


Fig. 11 A cut-out of brain sample undergoing small shear deformation

matter and determining the proper potential energy together with parameter identification seems desirable. However, such analysis is beyond the scope of this manuscript and shall be carried out in a separate contribution. For relevant studies on applications of peridynamics in biomechanics see [74–76].

7 Conclusion

Continuum-kinematics-inspired peridynamics (CPD) has been briefly introduced as a geometrically exact alternative to PD to formulate nonlocal continuum mechanics. Next, hyper-dual numbers and their underlying algebra were recapitulated and the associated differentiations with respect to scalar, vector and tensor arguments were elaborated. Based thereon, we developed a computational framework furnished

with automatic differentiation for implementation of CPD via employing hyper-dual numbers. The proposed computational framework is compact and model-independent, and suitable to incorporate any sophisticated material model via modifying the potential energy solely. Using the Seth–Hill strain measures, we proposed a family of internal potential energies that could be utilized for various material modelings. Through a set of numerical examples the performance and versatility of our proposed computational framework was evaluated while considering various loadings and material models. The convergence due to hyper-dual numbers proved to be highly accurate and identical to the one obtained by analytical derivations. The numerical implementation and solution procedure were robust and showed the asymptotically quadratic rate of convergence associated with the Newton–Raphson scheme. Taken together, differentiation

via hyper-dual numbers renders CPD as a compelling computational framework to study a broad variety of nonlocal materials.

Acknowledgements Ali Javili gratefully acknowledge the support provided by Scientific and Technological Research Council of Turkey (TÜBİTAK) Career Development Program, grant number 218M700. Paul Steinmann and Soheil Firooz gratefully acknowledge the support by the Deutsche Forschungsgemeinschaft (DFG, German Research Foundation) project number 460333672 – CRC 1540 Exploring Brain Mechanics (subproject C01).

Funding Open Access funding enabled and organized by Projekt DEAL.

Open Access This article is licensed under a Creative Commons Attribution 4.0 International License, which permits use, sharing, adaptation, distribution and reproduction in any medium or format, as long as you give appropriate credit to the original author(s) and the source, provide a link to the Creative Commons licence, and indicate if changes were made. The images or other third party material in this article are included in the article’s Creative Commons licence, unless indicated otherwise in a credit line to the material. If material is not included in the article’s Creative Commons licence and your intended use is not permitted by statutory regulation or exceeds the permitted use, you will need to obtain permission directly from the copyright holder. To view a copy of this licence, visit <http://creativecommons.org/licenses/by/4.0/>.

Appendix A: Numerical differentiation

In this section, various numerical differentiation methods are introduced and their associated error sources are highlighted and compared against each other. The most well-known numerical differentiation technique is the finite difference method. Aside from the finite difference method, complex, double and dual number systems have been developed to calculate the derivatives in a more accurate or a more simple fashion. These numbers were extended to hyper-complex, hyper-double and hyper-dual numbers in order to offer better accuracy for the calculation of second derivatives. Table 9 gathers all the aforementioned number systems together with their features. Assume x is a generic independent variable, $f(x)$ is a generic function and h is a real number. The Taylor series expansion of $f(x)$ reads

$$f(x + h) = f(x) + h \frac{\partial f(x)}{\partial x} + \frac{1}{2!} h^2 \frac{\partial^2 f(x)}{\partial x^2} + \frac{1}{3!} h^3 \frac{\partial^3 f(x)}{\partial x^3} + \dots, \tag{A.1}$$

with h being the perturbation value. In what follows, the performance of various numerical differentiation techniques is evaluated in approximating the first and second derivative of

our newly defined logarithmic potential energy which reads

$$\psi_1^{ai} = \psi_1^{ai}(x) = \frac{1}{2} C_1 |\Xi^{ai}| \ln \left(\frac{x}{|\Xi^{ai}|} \right), \tag{A.2}$$

with x being the independent parameter representing $|\xi^{ai}|$.

Appendix A.1: Finite difference method

Before elaborating on some advanced numerical differentiation methods, it is worthwhile to give a brief overview on the finite difference method in order to set the stage for further comparisons. There exist three main approaches to the finite difference method for the calculation of first and second derivatives. The first approach uses the backward difference formula which calculates the first and second derivatives of $f(x)$ as

$$\begin{aligned} \frac{\partial f(x)}{\partial x} &= \frac{f(x) - f(x - h)}{h} + \mathcal{O}(h) \quad \text{and} \\ \frac{\partial^2 f(x)}{\partial x^2} &= \frac{f(x) - 2f(x - h) + f(x - 2h)}{h^2} + \mathcal{O}(h). \end{aligned} \tag{A.3}$$

The second approach uses the forward difference formula which calculates the first and second derivatives of $f(x)$ as

$$\begin{aligned} \frac{\partial f(x)}{\partial x} &= \frac{f(x + h) - f(x)}{h} + \mathcal{O}(h) \quad \text{and} \\ \frac{\partial^2 f(x)}{\partial x^2} &= \frac{f(x + 2h) - 2f(x + h) + f(x)}{h^2} + \mathcal{O}(h). \end{aligned} \tag{A.4}$$

The third approach uses the central difference formula which offers higher accuracy and reads

$$\begin{aligned} \frac{\partial f(x)}{\partial x} &= \frac{f(x + h) - f(x - h)}{2h} + \mathcal{O}(h^2) \quad \text{and} \\ \frac{\partial^2 f(x)}{\partial x^2} &= \frac{f(x + h) - 2f(x) + f(x - h)}{h^2} + \mathcal{O}(h^2). \end{aligned} \tag{A.5}$$

Appendix A.2: Complex and hyper-complex numbers

For ordinary complex numbers [30, 31], the perturbation value takes the form ih with i the imaginary unit with the property $i^2 = -1$. Accordingly, the Taylor expansion of the function $f(x)$ takes the form

$$\begin{aligned} f(x + hi) &= f(x) + hi \frac{\partial f(x)}{\partial x} - \frac{1}{2!} h^2 \frac{\partial^2 f(x)}{\partial x^2} \\ &\quad - \frac{1}{3!} h^3 i \frac{\partial^3 f(x)}{\partial x^3} + \dots, \end{aligned} \tag{A.6}$$

Table 9 Summary of different number systems with their features

complex numbers	$\widehat{a} = a_0 + a_1i$	$i^2 = -1$	
hyper-complex numbers	$\widehat{a} = a_0 + a_1i_1 + a_2i_2 + a_{12}i_{12}$	$i_1^2 = i_2^2 = -1$	$i_{12} = i_{21} = i_1i_2 = i_2i_1 \neq 0$
double numbers	$\widetilde{a} = a_0 + a_1e$	$e^2 = +1$	
hyper-double numbers	$\widetilde{a} = a_0 + a_1e_1 + a_2e_2 + a_{12}e_{12}$	$e_1^2 = e_2^2 = +1$	$e_{12} = e_{21} = e_1e_2 = e_2e_1 \neq 0$
dual numbers	$\overline{a} = a_0 + a_1\epsilon$	$\epsilon^2 = 0$	
hyper-dual numbers	$\overline{a} = a_0 + a_1\epsilon_1 + a_2\epsilon_2 + a_{12}\epsilon_{12}$	$\epsilon_1^2 = \epsilon_2^2 = 0$	$\epsilon_{12} = \epsilon_{21} = \epsilon_1\epsilon_2 = \epsilon_2\epsilon_1 \neq 0$

that could be split in a real part and an imaginary part as

$$f(x + hi) = \left[f(x) - \frac{1}{2!}h^2 \frac{\partial^2 f(x)}{\partial x^2} + \dots \right] + \left[h \frac{\partial f(x)}{\partial x} - \frac{1}{3!}h^3 \frac{\partial^3 f(x)}{\partial x^3} + \dots \right] i. \quad (A.7)$$

Accordingly, the first and second derivatives of $f(x)$ can be calculated as

$$\begin{aligned} \frac{\partial f(x)}{\partial x} &= \frac{\Im(f(x + hi))}{h} + \mathcal{O}(h^2) \quad \text{and} \\ \frac{\partial^2 f(x)}{\partial x^2} &= \frac{2 \left[f(x) - \Re(f(x + hi)) \right]}{h^2} + \mathcal{O}(h^2). \end{aligned} \quad (A.8)$$

It is observed that for the first derivative, the subtractive cancellation error is eliminated whereas the truncation error still exist. The second derivative though, is subject to both subtractive cancellation and truncation errors.

Hyper-complex numbers are characterized by one real part and three non-real parts [77]. A hyper-complex number \widehat{a} is defined as

$$\widehat{a} = a_0 + a_1i_1 + a_2i_2 + a_{12}i_{12} \quad \text{with} \\ i_{12} = i_{21} = i_1i_2 = i_2i_1 \neq 0 \quad \text{and} \quad i_1^2 = i_2^2 = -1. \quad (A.9)$$

Accordingly, the real and non-real operators are defined as

$$\begin{aligned} \Re(\widehat{a}) &= \Re(a_0 + a_1i_1 + a_2i_2 + a_{12}i_{12}) = a_0, \\ \Im_{i_1}(\widehat{a}) &= \Im_{i_1}(a_0 + a_1i_1 + a_2i_2 + a_{12}i_{12}) = a_1, \\ \Im_{i_2}(\widehat{a}) &= \Im_{i_2}(a_0 + a_1i_1 + a_2i_2 + a_{12}i_{12}) = a_2, \\ \Im_{i_{12}}(\widehat{a}) &= \Im_{i_{12}}(a_0 + a_1i_1 + a_2i_2 + a_{12}i_{12}) = a_{12}, \end{aligned} \quad (A.10)$$

For the sake of simplicity, it is assumed that $a_1 = a_2 = h$ and $a_{12} = 0$ hence $\widehat{a} = a_0 + hi_1 + hi_2$. Therefore, the Taylor series expansion of the function $f(x + hi_1 + hi_2)$ reads

$$\begin{aligned} f(x + hi_1 + hi_2) &= f(x) + hi_1 \frac{\partial f(x)}{\partial x} + hi_2 \frac{\partial f(x)}{\partial x} \\ &\quad + \frac{1}{2!}2h^2[-1 + i_{12}] \frac{\partial^2 f(x)}{\partial x^2} \end{aligned}$$

$$- \frac{1}{3!}4h^3[i_1 + i_2] \frac{\partial^3 f(x)}{\partial x^3} + \dots, \quad (A.11)$$

that could be split into four parts as

$$\begin{aligned} f(x + hi_1 + hi_2) &= \left[f(x) - h^2 \frac{\partial^2 f(x)}{\partial x^2} \right] \\ &\quad + \left[h \frac{\partial f(x)}{\partial x} - \frac{1}{3!}4h^3 \frac{\partial^3 f(x)}{\partial x^3} + \dots \right] i_1 \\ &\quad + \left[h \frac{\partial f(x)}{\partial x} - \frac{1}{3!}4h^3 \frac{\partial^3 f(x)}{\partial x^3} + \dots \right] i_2 \\ &\quad + \left[h^2 \frac{\partial^2 f(x)}{\partial x^2} + \dots \right] i_{12}. \end{aligned} \quad (A.12)$$

The first and second derivatives of $f(x)$ can thus be calculated as

$$\begin{aligned} \frac{df(x)}{dx} &= \frac{\Im_{i_1}(f(x + hi_1 + hi_2))}{h} + \mathcal{O}(h^2) \\ &= \frac{\Im_{i_2}(f(x + hi_1 + hi_2))}{h} + \mathcal{O}(h^2) \quad \text{and} \\ \frac{\partial^2 f(x)}{\partial x^2} &= \frac{\Im_{i_{12}}(f(x + hi_1 + hi_2))}{h^2} + \mathcal{O}(h^2). \end{aligned} \quad (A.13)$$

Note that the operators \Im_{i_1} , \Im_{i_2} and $\Im_{i_{12}}$ extract the multiples to the non-real parts i_1 , i_2 and i_{12} , respectively. It is clear that upgrading the complex numbers to hyper-complex numbers eliminates the subtractive cancellation errors from second derivative whereas the truncation errors are still present.

Appendix A.3: Double and hyper-double numbers

Double numbers are distinguished from complex numbers via their non-real part [42]. For double numbers, the perturbation value takes the form he with e being the non-real part with the property $e^2 = +1$. Accordingly, the Taylor expansion of the function $f(x)$ takes the form

$$f(x + he) = f(x) + he \frac{\partial f(x)}{\partial x} + \frac{1}{2!}h^2 \frac{\partial^2 f(x)}{\partial x^2}$$

$$+ \frac{1}{3!} h^3 e \frac{\partial^3 f(x)}{\partial x^3} + \dots, \tag{A.14}$$

that could be split in a real part and a non-real part as

$$f(x + he) = \left[f(x) + \frac{1}{2!} h^2 \frac{\partial^2 f(x)}{\partial x^2} + \dots \right] + \left[h \frac{\partial f(x)}{\partial x} + \frac{1}{3!} h^3 \frac{\partial^3 f(x)}{\partial x^3} + \dots \right] e. \tag{A.15}$$

The first and second derivatives of $f(x)$ can thus be calculated as

$$\frac{df(x)}{\partial x} = \frac{\Im(f(x + he))}{h} + \mathcal{O}(h^2) \quad \text{and} \\ \frac{\partial^2 f(x)}{\partial x^2} = \frac{2 \left[\Re(f(x + he) - f(x)) \right]}{h^2} + \mathcal{O}(h^2). \tag{A.16}$$

Similar to the ordinary complex numbers, the first derivative is only subject to truncation error while the second derivative suffers from both subtractive cancellation and truncation errors.

Hyper-double numbers are characterized by one real part and three non-real parts. A hyper-double number \tilde{a} is defined as

$$\tilde{a} = a_0 + a_1 e_1 + a_2 e_2 + a_{12} e_{12} \quad \text{with} \\ e_{12} = e_{21} = e_1 e_2 = e_2 e_1 \neq 0 \quad \text{and} \quad e_1^2 = e_2^2 = 1. \tag{A.17}$$

Accordingly, the real and non-real operators are defined as

$$\Re(\tilde{a}) = \Re(a_0 + a_1 e_1 + a_2 e_2 + a_{12} e_{12}) = a_0, \\ \Im_{e_1}(\tilde{a}) = \Im_{e_1}(a_0 + a_1 e_1 + a_2 e_2 + a_{12} e_{12}) = a_1, \\ \Im_{e_2}(\tilde{a}) = \Im_{e_2}(a_0 + a_1 e_1 + a_2 e_2 + a_{12} e_{12}) = a_2, \\ \Im_{e_{12}}(\tilde{a}) = \Im_{e_{12}}(a_0 + a_1 e_1 + a_2 e_2 + a_{12} e_{12}) = a_{12}, \tag{A.18}$$

For the sake of simplicity, it is usually assumed that $a_1 = a_2 = h$ and $a_{12} = 0$ hence $\tilde{a} = a_0 + h e_1 + h e_2$. Therefore, the Taylor series expansion of the function $f(x + h e_1 + h e_2)$ reads

$$f(x + h e_1 + h e_2) = f(x) + h e_1 \frac{\partial f(x)}{\partial x} + h e_2 \frac{\partial f(x)}{\partial x} + \frac{1}{2!} 2 h^2 [1 + e_{12}] \frac{\partial^2 f(x)}{\partial x^2} + \frac{1}{3!} 4 h^3 [e_1 + e_2] \frac{\partial^3 f(x)}{\partial x^3} + \dots, \tag{A.19}$$

that could be split into four parts as

$$f(x + h e_1 + h e_2) = \left[f(x) + h^2 \frac{\partial^2 f(x)}{\partial x^2} \right] + \left[h \frac{\partial f(x)}{\partial x} + \frac{1}{3!} 4 h^3 \frac{\partial^3 f(x)}{\partial x^3} + \dots \right] e_1 + \left[h \frac{\partial f(x)}{\partial x} + \frac{1}{3!} 4 h^3 \frac{\partial^3 f(x)}{\partial x^3} + \dots \right] e_2 + \left[h^2 \frac{\partial^2 f(x)}{\partial x^2} + \dots \right] e_{12}. \tag{A.20}$$

The first and second derivatives of $f(x)$ can thus be calculated as

$$\frac{df(x)}{\partial x} = \frac{\Im_{e_1}(f(x + h e_1 + h e_2))}{h} + \mathcal{O}(h^2) \\ = \frac{\Im_{e_2}(f(x + h e_1 + h e_2))}{h} + \mathcal{O}(h^2) \quad \text{and} \\ \frac{\partial^2 f(x)}{\partial x^2} = \frac{\Im_{e_{12}}(f(x + h e_1 + h e_2))}{h^2} + \mathcal{O}(h^2). \tag{A.21}$$

Note that the operators \Im_{e_1} , \Im_{e_2} and $\Im_{e_{12}}$ extract the multiples to the non-real parts e_1 , e_2 and e_{12} , respectively. It is clear that upgrading the double numbers to hyper-double numbers eliminates the subtractive cancellation errors for both first and second derivatives whereas the truncation errors are still present.

Appendix A.4: Dual and hyper-dual numbers

Dual numbers are distinguished from complex numbers via their non-real or non-real part [32]. For dual numbers, the perturbation value takes the form $h\epsilon$ with ϵ being the non-real part with the property $\epsilon^2 = 0$. Accordingly, the Taylor expansion of the function $f(x)$ takes the form

$$f(x + h\epsilon) = f(x) + h\epsilon \frac{\partial f(x)}{\partial x}, \tag{A.22}$$

consisting of a real and a non-real part. Note, in this case, the Taylor expansion of the function itself does not suffer from any truncation error. Subsequently, the first derivative of $f(x)$ can be calculated as

$$\frac{\partial f(x)}{\partial x} = \frac{\Im(f(x + h\epsilon))}{h}. \tag{A.23}$$

Although both subtractive cancellation error and truncation error are eliminated for the first derivatives of $f(x)$, the second derivatives cannot be calculated due to the vanishing higher order terms in the Taylor expansion.

Table 10 Summary of the performance of the numerical differentiation methods in terms of error sources

differentiation method	first derivative		second derivative	
	subtractive cancellation error	truncation error	subtractive cancellation error	truncation error
finite difference method	✗	✗	✗	✗
complex numbers	✓	✗	✗	✗
hyper-complex numbers	✓	✗	✓	✗
double numbers	✓	✗	✗	✗
hyper-double numbers	✓	✗	✓	✗
dual numbers	✓	✓	—	—
hyper-dual numbers	✓	✓	✓	✓

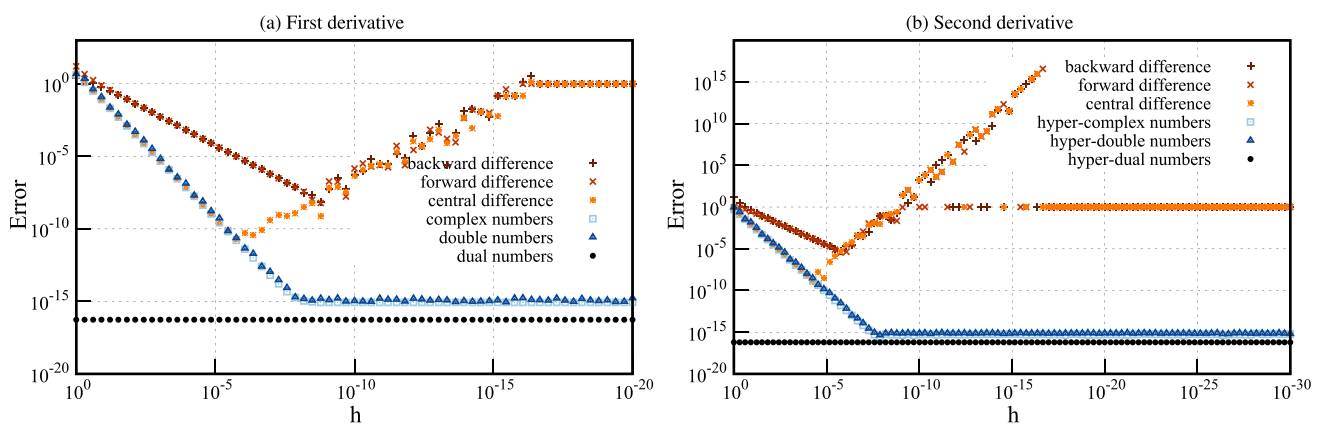


Fig. 12 Comparison of various numerical differentiation methods in calculation of first and second derivatives

The hyper-dual numbers are characterized with one real part and three non-real parts. A hyper-dual number \bar{a} is defined as

$$\bar{a} = a_0 + a_1\epsilon_1 + a_2\epsilon_2 + a_{12}\epsilon_{12} \quad \text{with} \\ \epsilon_{12} = \epsilon_{21} = \epsilon_1\epsilon_2 = \epsilon_2\epsilon_1 \neq 0 \quad \text{and} \quad \epsilon_1^2 = \epsilon_2^2 = 0. \quad (\text{A.24})$$

Accordingly, the real and non-real operators are defined as

$$\Re(\bar{a}) = \Re(a_0 + a_1\epsilon_1 + a_2\epsilon_2 + a_{12}\epsilon_{12}) = a_0, \\ \Im_{\epsilon_1}(\bar{a}) = \Im_{\epsilon_1}(a_0 + a_1\epsilon_1 + a_2\epsilon_2 + a_{12}\epsilon_{12}) = a_1, \\ \Im_{\epsilon_2}(\bar{a}) = \Im_{\epsilon_2}(a_0 + a_1\epsilon_1 + a_2\epsilon_2 + a_{12}\epsilon_{12}) = a_2, \\ \Im_{\epsilon_{12}}(\bar{a}) = \Im_{\epsilon_{12}}(a_0 + a_1\epsilon_1 + a_2\epsilon_2 + a_{12}\epsilon_{12}) = a_{12}. \quad (\text{A.25})$$

For the sake of simplicity, it is usually assumed that $a_1 = a_2 = h$ and $a_{12} = 0$ hence $\bar{a} = a_0 + h\epsilon_1 + h\epsilon_2$. Therefore,

the Taylor series expansion of the function $f(x + h\epsilon_1 + h\epsilon_2)$ reads

$$f(x + h\epsilon_1 + h\epsilon_2) = f(x) + h\epsilon_1 \frac{\partial f(x)}{\partial x} + h\epsilon_2 \frac{\partial f(x)}{\partial x} + h^2\epsilon_{12} \frac{\partial^2 f(x)}{\partial x^2}, \quad (\text{A.26})$$

that could be rewritten as

$$f(x + h\epsilon_1 + h\epsilon_2) = f(x) + \left[h \frac{\partial f(x)}{\partial x} \right] \epsilon_1 + \left[h \frac{\partial f(x)}{\partial x} \right] \epsilon_2 + \left[h^2 \frac{\partial^2 f(x)}{\partial x^2} \right] \epsilon_{12}, \quad (\text{A.27})$$

The first and second derivatives of $f(x)$ can be calculated as

$$\begin{aligned} \frac{\partial f(x)}{\partial x} &= \frac{\mathfrak{S}_{\epsilon_1}(f(x + h\epsilon_1 + h\epsilon_2))}{h} \\ &= \frac{\mathfrak{S}_{\epsilon_2}(f(x + h\epsilon_1 + h\epsilon_2))}{h} \quad \text{and} \\ \frac{\partial^2 f(x)}{\partial x^2} &= \frac{\mathfrak{S}_{\epsilon_{12}}(f(x + h\epsilon_1 + h\epsilon_2))}{h^2}. \end{aligned} \tag{A.28}$$

Note that the operators $\mathfrak{S}_{\epsilon_1}$, $\mathfrak{S}_{\epsilon_2}$ and $\mathfrak{S}_{\epsilon_{12}}$ extract the multiples to the non-real parts ϵ_1 , ϵ_1 and ϵ_{12} , respectively. It is observed that the first and the second derivatives suffer from neither truncation errors nor subtractive cancellation errors. As a result, both derivatives are calculated in an exact manner. Table 10 gathers all the aforementioned numerical differentiation methods and the types of errors they suffer from (Fig. 12). Figure 12 compares the performance of the presented numerical differentiation techniques in approximating the first and second derivative of potential energy defined in Eq. A.2

Appendix B: Derivatives of CPD deformation measures

Suppose $\{\bullet\}$ is an arbitrary variable and its derivation with respect to the point \mathbf{x}^b is sought. Depending on the relative deformation measures $\{\bullet\}$, three different possibilities exist. If $\{\bullet\}$ depends on one relative deformation measure ξ^{ai} , we have

$$\begin{aligned} \frac{\partial \{\bullet\}}{\partial \mathbf{x}^b} &= \frac{\partial \{\bullet\}}{\partial \xi^{ai}} \cdot \frac{\partial \xi^{ai}}{\partial \mathbf{x}^b} = \frac{\partial \{\bullet\}}{\partial \xi^{ai}} \cdot \frac{\partial [\mathbf{x}^i - \mathbf{x}^a]}{\partial \mathbf{x}^b} \\ &= \frac{\partial \{\bullet\}}{\partial \xi^{ai}} \cdot \left[\frac{\partial \mathbf{x}^i}{\partial \mathbf{x}^b} - \frac{\partial \mathbf{x}^a}{\partial \mathbf{x}^b} \right] \\ &= \frac{\partial \{\bullet\}}{\partial \xi^{ai}} \cdot \left[[\delta^{ib} - \delta^{ab}] \mathbf{i} \right] = [\delta^{ib} - \delta^{ab}] \frac{\partial \{\bullet\}}{\partial \xi^{ai}}. \end{aligned} \tag{B.1}$$

If $\{\bullet\}$ depends on two relative deformation measures ξ^{ai} and ξ^{aj} , we have

$$\begin{aligned} \frac{\partial \{\bullet\}}{\partial \mathbf{x}^b} &= \frac{\partial \{\bullet\}}{\partial \xi^{ai}} \cdot \frac{\partial \xi^{ai}}{\partial \mathbf{x}^b} + \frac{\partial \{\bullet\}}{\partial \xi^{aj}} \cdot \frac{\partial \xi^{aj}}{\partial \mathbf{x}^b} = \frac{\partial \{\bullet\}}{\partial \xi^{ai}} \cdot \left[[\delta^{ib} - \delta^{ab}] \mathbf{i} \right] \\ &+ \frac{\partial \{\bullet\}}{\partial \xi^{aj}} \cdot \left[[\delta^{jb} - \delta^{ab}] \mathbf{i} \right] = [\delta^{ib} - \delta^{ab}] \frac{\partial \{\bullet\}}{\partial \xi^{ai}} \\ &+ [\delta^{jb} - \delta^{ab}] \frac{\partial \{\bullet\}}{\partial \xi^{aj}}, \end{aligned} \tag{B.2}$$

and finally if $\{\bullet\}$ depends on three relative deformation measures ξ^{ai} , ξ^{aj} and ξ^{ak} , we have

$$\begin{aligned} \frac{\partial \{\bullet\}}{\partial \mathbf{x}^b} &= \frac{\partial \{\bullet\}}{\partial \xi^{ai}} \cdot \frac{\partial \xi^{ai}}{\partial \mathbf{x}^b} + \frac{\partial \{\bullet\}}{\partial \xi^{aj}} \cdot \frac{\partial \xi^{aj}}{\partial \mathbf{x}^b} + \frac{\partial \{\bullet\}}{\partial \xi^{ak}} \cdot \frac{\partial \xi^{ak}}{\partial \mathbf{x}^b} \\ &= \frac{\partial \{\bullet\}}{\partial \xi^{ai}} \cdot \left[[\delta^{ib} - \delta^{ab}] \mathbf{i} \right] + \frac{\partial \{\bullet\}}{\partial \xi^{aj}} \cdot \left[[\delta^{jb} - \delta^{ab}] \mathbf{i} \right] \\ &+ \frac{\partial \{\bullet\}}{\partial \xi^{ak}} \cdot \left[[\delta^{kb} - \delta^{ab}] \mathbf{i} \right] \\ &= [\delta^{ib} - \delta^{ab}] \frac{\partial \{\bullet\}}{\partial \xi^{ai}} + [\delta^{jb} - \delta^{ab}] \frac{\partial \{\bullet\}}{\partial \xi^{aj}} \\ &+ [\delta^{kb} - \delta^{ab}] \frac{\partial \{\bullet\}}{\partial \xi^{ak}}, \end{aligned} \tag{B.3}$$

Accordingly we have

$$\begin{aligned} \frac{\partial \xi^{ai}}{\partial \mathbf{x}^b} &= [\delta^{ib} - \delta^{ab}] \frac{\partial \xi^{ai}}{\partial \xi^{ai}} = [\delta^{ib} - \delta^{ab}] \mathbf{i}, \\ \frac{\partial [\xi^{ai} \times \xi^{aj}]}{\partial \mathbf{x}^b} &= [\delta^{ib} - \delta^{ab}] \frac{\partial [\xi^{ai} \times \xi^{aj}]}{\partial \xi^{ai}} \\ &+ [\delta^{jb} - \delta^{ab}] \frac{\partial [\xi^{ai} \times \xi^{aj}]}{\partial \xi^{aj}} \\ &= [\delta^{ib} - \delta^{ab}] [\xi^{aj} \cdot \mathbf{e}] \\ &+ [\delta^{jb} - \delta^{ab}] [\xi^{ai} \cdot \mathbf{e}], \\ \frac{\partial [\xi^{ai} \cdot [\xi^{aj} \times \xi^{ak}]]}{\partial \mathbf{x}^b} &= [\delta^{ib} - \delta^{ab}] \frac{\partial [\xi^{ai} \cdot [\xi^{aj} \times \xi^{ak}]]}{\partial \xi^{ai}} \\ &+ [\delta^{jb} - \delta^{ab}] \frac{\partial [\xi^{ai} \cdot [\xi^{aj} \times \xi^{ak}]]}{\partial \xi^{aj}} \\ &+ [\delta^{kb} - \delta^{ab}] \frac{\partial [\xi^{ai} \cdot [\xi^{aj} \times \xi^{ak}]]}{\partial \xi^{ak}} \\ &= [\delta^{ib} - \delta^{ab}] [\xi^{aj} \times \xi^{ak}] \\ &+ [\delta^{jb} - \delta^{ab}] [\xi^{ak} \times \xi^{ai}] \\ &+ [\delta^{kb} - \delta^{ab}] [\xi^{ai} \times \xi^{aj}]. \end{aligned} \tag{B.4}$$

References

1. Silling SA (2000) Reformulation of elasticity theory for discontinuities and long-range forces. *J Mech Phys Solids* 48:175–209
2. Silling SA, Lehoucq RB (2010) Peridynamic theory of solid mechanics. *Adv Appl Mech* 44:73–168
3. Silling SA, Epton M, Weckner O, Xu J, Askari E (2007) Peridynamic states and constitutive modeling, 88
4. Madenci E, Oterkus E (2014) *Peridynamics theory and its applications*, vol 91. Springer
5. Frieberthäuser K, Werner M, Weinberg K (2022) Dynamic fracture with continuum-kinematics-based peridynamics. *AIMS Mater Sci* 9:791–807

6. Khosravani MR, Friebertshäuser K, Weinberg K (2022) On the use of peridynamics in fracture of ultra-high performance concrete. *Mech Res Commun* 123:103899
7. Nguyen CT, Oterkus S, Oterkus E (2021) An energy-based peridynamic model for fatigue cracking. *Eng Fract Mech* 241:107373
8. Wang H, Oterkus E, Oterkus S (2018) Predicting fracture evolution during lithiation process using peridynamics. *Eng Fract Mech* 192:176–191
9. Vazic B, Wang H, Diyaroglu C, Oterkus S, Oterkus E (2017) Dynamic propagation of a macrocrack interacting with parallel small cracks. *AIMS Mater Sci* 4:118–136
10. Javili A, Morasata R, Oterkus E, Oterkus S (2019) Peridynamics review. *Math Mech Solids* 24:3714–3739
11. Hattori G, Trevelyan J, Coombs WM (2018) A non-ordinary state-based peridynamics framework for anisotropic materials. *Comput Methods Appl Mech Eng* 339:416–442
12. Javili A, McBride AT, Steinmann P (2019) Continuum-kinematics-inspired peridynamics. *Mechanical problems. J Mech Phys Solids* 131:125–146
13. Javili A, Firooz S, McBride AT, Steinmann P (2020) The computational framework for continuum-kinematics-inspired peridynamics. *Comput Mech* 66:795–824
14. Javili A, McBride AT, Steinmann P (2021) A geometrically exact formulation of peridynamics. *Theoret Appl Fract Mech* 111:102850
15. Javili A, Ekiz E, McBride AT, Steinmann P (2021) Continuum-kinematics-inspired peridynamics: thermo-mechanical problems. *Continuum Mech Thermodyn* 33:2039–2063
16. Schaller E, Javili A, Steinmann P (2022) Open system peridynamics. *Continuum Mech Thermodyn* 34:1125–1141
17. Zhou XP, Tian DL (2021) A novel linear elastic constitutive model for continuum-kinematics-inspired peridynamics. *Comput Methods Appl Mech Eng* 373:113479
18. Ekiz E, Steinmann P, Javili A (2022) Relationships between the material parameters of continuum-kinematics-inspired peridynamics and isotropic linear elasticity for two-dimensional problems. *Int J Solids Struct* 238:111366
19. Ekiz E, Steinmann P, Javili A (2022) From two- to three-dimensional continuum-kinematics-inspired peridynamics: more than just another dimension. *Mech Mater* 173:104417
20. Laurien M, Javili A, Steinmann P (2021) Nonlocal wrinkling instabilities in bilayered systems using peridynamics. *Comput Mech* 68:1023–1037
21. Schaller E, Javili A, Schmidt I, Papastavrou A, Steinmann P (2022) A peridynamic formulation for nonlocal bone remodelling. *Comput Methods Biomech Biomed Engin* 25:1835–1851
22. Javili A, McBride AT, Mergheim J, Steinmann P (2021) Towards elasto-plastic continuum-kinematics-inspired peridynamics. *Comput Methods Appl Mech Eng* 380:113809
23. Tian DL, Zhou XP (2021) A continuum-kinematics-inspired peridynamic model of anisotropic continua: elasticity, damage, and fracture. *Int J Mech Sci* 199:106413
24. Friebertshäuser K, Thomas M, Tornquist S, Weinberg K, Wieners C (2023) Dynamic fracture with a continuum-kinematics-based peridynamic and a phase-field approach. *Proc Appl Math Mech* 22(1):e202200217
25. Laurien M, Javili A, Steinmann P (2022) A nonlocal interface approach to peridynamics exemplified by continuum-kinematics-inspired peridynamics. *Int J Numer Meth Eng* 123:3464–3484
26. Laurien M, Javili A, Steinmann P (2022) Peridynamic modeling of nonlocal degrading interfaces in composites. *Forces Mech* 10:100124
27. Pérez-Foguet A, Rodríguez-Ferran A, Huerta A (2000) Numerical differentiation for local and global tangent operators in computational plasticity. *Comput Methods Appl Mech Eng* 189:277–296
28. Sun W, Chaikof EL, Levenston ME (2008) Numerical approximation of tangent moduli for finite element implementations of nonlinear hyperelastic material models. *J Biomech Eng* 130:061003
29. Martins JRRA, Hwang JT (2013) Review and unification of methods for computing derivatives of multidisciplinary computational models. *AIAA J* 51:2582–2599
30. Martins JRRA, Kroo IM, Alonso JJ (2000) An automated method for sensitivity analysis using complex variables, In: 38th Aerospace Sciences Meeting and Exhibit
31. Martins JRRA, Sturdza P, Alonso JJ (2003) The complex-step derivative approximation. *ACM Transact Math Soft* 29:245–262
32. Study E (1891) Von den Bewegungen und Umlegungen. *Math Ann* 39:441–565. <https://doi.org/10.1007/bf01199824>
33. Kim S, Ryu J, Cho M (2011) Numerically generated tangent stiffness matrices using the complex variable derivative method for nonlinear structural analysis. *Comput Methods Appl Mech Eng* 200:403–413
34. Lai KL, Crassidis JL (2008) Extensions of the first and second complex-step derivative approximations. *J Comput Appl Math* 219:276–293
35. Keler ML (1973) Kinematics and statics including friction in single-loop mechanisms by screw calculus and dual vectors. *J Eng Industry* 95:471–480
36. Veldkamp GR (1976) On the use of dual numbers, vectors and matrices in instantaneous, spatial kinematics. *Mech Mach Theory* 11:141–156
37. Kiran R, Khandelwal K (2014) Complex step derivative approximation for numerical evaluation of tangent moduli. *Comput Struct* 140:1–13
38. Brodsky V, Shoham M (1999) Dual numbers representation of rigid body dynamics. *Mech Mach Theory* 34:693–718
39. Pennestri E, Stefanelli R (2007) Linear algebra and numerical algorithms using dual numbers. *Multibody SysDyn* 18:323–344
40. Laue S (2019) On the equivalence of forward mode automatic differentiation and symbolic differentiation, arXiv preprint
41. Fike JA, Alonso J (2011) The development of hyper-dual numbers for exact second-derivative calculations, In: 49th AIAA Aerospace Sciences Meeting including the New Horizons Forum and Aerospace Exposition, pp. 1–17
42. Clifford C (1871) Preliminary sketch of biquaternions. *Proc Lond Math Soc* 1:381–395
43. Fike JA, Jongsma S, Alonso JJ, van der Weide E (2011) Optimization with gradient and hessian information calculated using hyper-dual numbers, In: 29th AIAA Applied Aerodynamics Conference, pp. 1–19
44. Imoto Y, Yamanaka N, Uramoto T, Tanaka M, Fujikawa M, Mitsuume N (2020) Fundamental theorem of matrix representations of hyper-dual numbers for computing higher-order derivatives. *JSIAM Lett* 12:29–32
45. Cohen A, Shoham M (2018) Principle of transference—an extension to hyper-dual numbers. *Mech Mach Theory* 125:101–110
46. Endo VT, Fancello EA, Muñoz-Rojas PA (2021) Second-order design sensitivity analysis using diagonal hyper-dual numbers. *Int J Numer Meth Eng* 122:7134–7155
47. Kiran R, Khandelwal K (2015) Automatic implementation of finite strain anisotropic hyperelastic models using hyper-dual numbers. *Comput Mech* 55:229–248
48. Tanaka M, Sasagawa T, Omote R, Fujikawa M, Balzani D, Schröder J (2015) A highly accurate 1st- and 2nd-order differentiation scheme for hyperelastic material models based on hyper-dual numbers. *Comput Methods Appl Mech Eng* 283:22–45
49. Tanaka M, Balzani D, Schröder J (2016) Implementation of incremental variational formulations based on the numerical calculation of derivatives using hyper dual numbers. *Comput Methods Appl Mech Eng* 301:216–241

50. Cohen A, Shoham M (2016) Application of hyper-dual numbers to multibody kinematics. *J Mech Robot* 8:2–5
51. Cohen A, Shoham M (2020) Hyper dual quaternions representation of rigid bodies kinematics. *Mech Mach Theory* 150:103861
52. Cohen A, Shoham M (2017) Application of hyper-dual numbers to rigid bodies equations of motion. *Mech Mach Theory* 111:76–84
53. Rehner P, Bauer G (2021) Application of generalized (Hyper-) dual numbers in equation of state modeling. *Front Chem Eng* 3:1–7
54. Brake MRW, Fike JA, Topping SD (2016) Parameterized reduced order models from a single mesh using hyper-dual numbers. *J Sound Vib* 371:370–392
55. Fujii F, Tanaka M, Sasagawa T, Omote R (2017) Computational two-mode asymptotic bifurcation theory combined with hyper dual numbers and applied to plate/shell buckling. *Comput Methods Appl Mech Eng* 325:666–688
56. Fohrmeister V, Bartels A, Mosler J (2018) Variational updates for thermomechanically coupled gradient-enhanced elastoplasticity – Implementation based on hyper-dual numbers. *Comput Methods Appl Mech Eng* 339:239–261
57. Murai D, Omote R, Tanaka M (2022) The method for solving topology optimization problems using hyper-dual numbers. *Arch Appl Mech* 92:2813–2824
58. Bonney MS, Kammer DC, Brake MRW (2015) Fully parameterized reduced order models using hyper-dual numbers and component mode synthesis. In: *Proceedings of the ASME 2015 International Design Engineering Technical Conferences and Computers and Information in Engineering Conference*, pp. 1–7
59. Wang L, Abeyaratne R (2018) A one-dimensional peridynamic model of defect propagation and its relation to certain other continuum models. *J Mech Phys Solids* 116:334–349
60. Thevamaran R, Fraternali F, Daraio C (2014) Multiscale mass-spring model for high-rate compression of vertically aligned carbon nanotube foams. *J Appl Mech* 81:121006
61. Nadkarni N, Daraio C, Kochmann DM (2014) Dynamics of periodic mechanical structures containing bistable elastic elements: from elastic to solitary wave propagation. *Phys Rev E* 90:023204
62. Scott AC (1969) A Nonlinear Klein-Gordon Equation. *Am J Phys* 37:52–61
63. Bishop AR, Lewis WF (1979) A theory of intrinsic coercivity in narrow magnetic domain wall materials. *J Mech Phys Solids* 12:3811–3825
64. Rotermund HH, Jakubith S, von Oertzen A, Ertl G (1991) Solitons in a surface reaction. *Phys Rev Lett* 66:3083–3088
65. Brothers MD, Foster JT, Millwater HR (2014) A comparison of different methods for calculating tangent-stiffness matrices in a massively parallel computational peridynamics code. *Comput Methods Appl Mech Eng* 279:247–267
66. Littlewood D (2015) Roadmap for software implementation, Tech. Rep. October, Sandia National Lab
67. Bode T (2021) Peridynamic Galerkin methods for nonlinear solid mechanics, Ph.D. thesis, Gottfried Wilhelm Leibniz Universität Hannover
68. Bode T, Weißenfels C (2020) Wriggers, Peridynamic petrov-galerkin method: a generalization of the peridynamic theory of correspondence materials. *Comput Methods Appl Mech Eng* 358:112636
69. Rothe S, Hartmann S (2015) Automatic differentiation for stress and consistent tangent computation. *Arch Appl Mech* 85:1103–1125
70. Saeb S, Steinmann P, Javili A (2016) Aspects of computational homogenization at finite deformations: a unifying review from Reuss’ to Voigt’s Bound. *Appl Mech Rev* 68:050801
71. Budday S, Nay R, de Rooij R, Steinmann P, Wyrobek T, Ovaert TC, Kuhl E (2015) Mechanical properties of gray and white matter brain tissue by indentation. *J Mech Behav Biomed Mater* 46:318–330
72. Budday S, Sommer G, Birkl C, Langkammer C, Haybaeck J, Kohnert J, Bauer M, Paulsen F, Steinmann P, Kuhl E et al (2017) Mechanical characterization of human brain tissue. *Acta Biomater* 48:319–340
73. Budday S, Ovaert TC, Holzapfel GA, Steinmann P, Kuhl E (2020) Fifty shades of brain: a review on the mechanical testing and modeling of brain tissue. *Arch Comput Methods Eng* 27:1187–1230
74. Lejeune E, Linder C (2017) Modeling tumor growth with peridynamics. *Biomech Model Mechanobiol* 16:1141–1157
75. Lejeune E, Linder C (2018) Modeling mechanical inhomogeneities in small populations of proliferating monolayers and spheroids. *Biomech Model Mechanobiol* 17:727–743
76. Lejeune E, Linder C (2021) Modeling biological materials with peridynamics, In: *Peridynamic Modeling, Numerical Techniques, and Applications*, Elsevier, pp. 249–273
77. Lantoine G, Russell RP, Dargent T (2012) Using multicomplex variables for automatic computation of high-order derivatives. *ACM Transact Math Soft* 38:1–21

Publisher’s Note Springer Nature remains neutral with regard to jurisdictional claims in published maps and institutional affiliations.